Light Backscattering by Atmospheric Particles: From Laboratory to Field Experiments

A. Miffre

Abstract Atmospheric particles may somewhat counterbalance the global warming effect of the Earth's atmosphere due to greenhouse gases by directly contributing to the Earth's climate through light scattering and absorption processes. According to the IPCC report (IPCC in Climate change 2013: the physical science basis. New York: Cambridge Univ. Press, 2013), the contribution of such particles to the Earth's radiative budget however remains difficult to handle and quantify, mainly due to the complexity of these particles, which present a wide range of sizes, shapes and complex refractive indices. To face such a complexity, a major source of global data on these particles is provided by ground-based and satellite-based lidar remote sensing instruments, which are based on light backscattering and extinction by atmospheric particles. In this context, this book chapter proposes to present some recent advances in the field of light backscattering by complex-shaped atmospheric particles at specific backward scattering angle ($\theta = \pi$) at which lidar instruments operate, for the first time to our knowledge in laboratory where a π-polarimeter has been built and operated for aerosols (Miffre et al. in J Quant Spectrosc Radiat Transf 169:79–90, 2016; Miffre et al. in J Quant Spectrosc Radiat Transf 222–223:45–59, 2019b; Miffre et al. Atmos Meas Tech, 2022). These papers are the results of a team work in which Prof. Rairoux's expertise in lidar remote sensing and laser spectroscopy played a key role. This work also owes much to former PhD students, G. David and D. Cholleton, who also played a key role. Laboratory experiments at near ($\theta < \pi$) backscattering angles are likewise proposed in complement as well as cooperative works with ONERA (Paulien et al. in J Quant Spectrosc Radiat Transf 260, 2021) and chemical colleagues from Lyon University (France) and North Carolina University (USA) (Dubois et al. in Phys Chem Chem Phys 23:5927–5935, 2021) to explore light backscattering by complex-shaped particles. The benefits of this new laboratory approach, in comparison with existing light scattering numerical simulations and lidar field experiments, is discussed. We hope this book chapter will improve

---

A. Miffre (✉)
University of Lyon, Université Claude Bernard Lyon 1, CNRS, Institut Lumière Matière, F-69622, Villeurbanne, France
e-mail: alain.miffre@univ-lyon1.fr

A. Kokhanovsky (ed.), *Springer Series in Light Scattering*, Springer Series in Light Scattering, https://doi.org/10.1007/978-3-031-10298-1_5

our understanding of the complex physical process of light backscattering by atmospheric particles, to in turn improve our understanding of the radiative properties of complex-shaped atmospheric particles, to provide answer to radiative transfer issues.

1 Introduction

1.1 *On the Complexity of Atmospheric Particles*

The Earth's atmosphere is composed of particles which are extremely complex in size, shape and chemical composition (Mishchenko et al. 2002; Seinfeld and Pandis 2006). While the particles size may vary from a few nanometers (soot monomers) to several micrometers (for pollen), the particles shape is generally highly irregular, sometimes with sharp edges, as for mineral dust. Atmospheric particles are also potentially highly inhomogeneous (Kahnert 2015; Liu et al. 2014; Mishchenko et al. 2013) and may present a rough surface (Kahnert and Rother 2011; Kemppinen et al. 2015; Zubko et al. 2007). Figure 1 highlights the complexity in size and shape of several of such particles, through their laboratory TEM- images.

This situation is obviously much more complex in the atmosphere, where these particles are not isolated but may interact through a complex chemistry (Seinfeld and Pandis 2006) and form particle mixtures (Mishchenko et al. 2004a, b). During advection transport from source regions to remote places where intrusion episodes occur, freshly emitted particles indeed experience chemical reactivity, including potential humidification, possible scavenging, sedimentation processes, water adsorption at the particles surface which may strongly influence their size and their shape. Largest particles, for sizes in the range of ten micrometers, are rapidly removed by gravitational settling. In contrast, finer particles with longer residence times in the Earth's atmosphere, may be transported over large distances and may remain in the troposphere for several weeks (Ovadnevaite et al. 2009) which further reinforce their radiative impact by affecting the Earth's climate at both local, regional and global scales. Hence, after long-range transport, atmospheric particles are highly dispersed and aged, and may present sizes and shapes that can be very different from those observed in the source region. As a result, the vertical layering generally observed at far-range remote sites where intrusion episodes occur is itself complex and has to

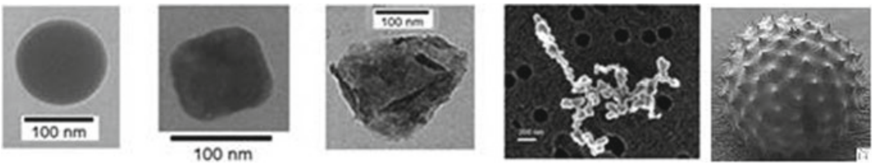

Fig. 1 Atmospheric particles TEM-images (from left to right, taken at iLM): ammonium sulfate, sea-salt below crystallization point, Arizona test dust, soot aggregate, ragweed pollen

be accurately analysed to quantify the Earth's energy balance. For accurate radiative forcing assessments, the particles non-sphericity should be taken into account, by including the particles inhomogeneity. Among the major uncertainties involved in climate change modeling, the lack of knowledge on the atmospheric particles shape is indeed an essential point: non-spherical particles are particularly challenging, because there is no generic, exact light scattering theory for such complex-shaped particles (Kahnert et al. 2014; Mishchenko 2009), except for some specific geometries far away from the observed highly-irregularly shape of atmospheric particles (Mishchenko et al. 2002). Hence, while atmospheric particles contribute to the Earth's radiative budget directly through light scattering and extinction (Mishchenko et al. 2002), applying the century-old Lorenz-Mie theory to such complex-shaped particles may lead to significant errors in aerosol climate forcing and radiance computations, as non-spherical particles scatter light differently from volume or surface-equivalent spheres (Kahnert et al. 2007). In particular, orientation averaging over an ensemble of non-spherical particles does not lead to the same scattering pattern as for spheres (Nousiainen 2009). In conclusion, there is no analytical solution of the Maxwell's equations exists for light-scattering by these particles, which are hard to represent mathematically in climate models. Only recently (Räisänen et al. 2013), climate models started to account for the non-sphericity of atmospheric aerosols by considering spheroids. As a result, light scattering and absorption has to be quantified by taking into account the particles nonsphericity. This is especially true for the specific backward scattering direction, at which most climate satellites operate, including those involving lidar remote sensing instruments such as the CALIPSO mission (Winker et al. 2003).

1.2 On the Importance of Light Backscattering by Atmospheric Particles

To face such a complexity and improve our understanding of the Earth's climate, a powerful methodology is to take benefit from light backscattering by atmospheric particles. Following Mishchenko's text book (Mishchenko et al. 2002), elastic light scattering is the physical process by which particles "*extract some of the incident energy and scatter it in all directions at the frequency of the incident beam, generally giving rise to a polarization state different from that of the incident beam*". In this book chapter, we will focus on elastic light backscattering by atmospheric particles. By light backscattering, we here intend light scattering in the exact (i.e., strict) backward scattering direction of π or 180.0°, hence far from the 90 to 170° scattering angles, sometimes reported in the literature as backward scattering direction. Light scattering may indeed vary when the scattering angle differs from the exact π-backscattering angle. Among all light scattering directions, the backward scattering direction has drawn attention for both practical and fundamental reasons. The motivations for this work, dedicated on light backscattering by atmospheric particles, are hence the following:

- Basically, light backscattering has proven efficiency for providing information on the optical properties of condensed or gaseous matter, with numerous applications in various research fields, such as biomedicine (Vitkin and Studinski 2001; Wang et al. 2012) or fundamental research (Wiersma et al. 1997). This approach should be extended to particles in dilute media such as aerosols. This is especially true for sulfate particles as sulfate particles induce a net cooling of the Earth's atmosphere due to their ability to backscatter light (Dubois et al. 2021). Light backscattering is also important from a more fundamental point of view, as it may lead to the so-called coherent backscattering (Mishchenko et al. 2002). Also, as noted in (Fu et al. 2017), the backward scattering direction has been identified as one of the most sensitive directions to the particles heterogeneities and surface structure, including possible surface roughness. Hence, as discussed in (Kemppinen et al. 2015) through numerical simulations, the most prominent effects of surface roughness are seen close to the exact backscattering direction and the diagonal scattering matrix elements are affected the most in the backscattering direction. We could then investigate the influence of surface roughness on lidar backscattering profiles (Mehri et al. 2018). Also, near the backward scattering direction, light scattering numerical simulations exhibit a narrow double-lobe feature when studying small-scale surface roughness (Kahnert et al. 2012). Finally, for radiative transfer purposes, the scattering phase function needs to be precisely known over the whole scattering angle range, and hence covers the backward scattering direction with precision.
- Practically speaking, light backscattering is involved in ground-based and satellite-based lidar remote sensing instruments which provide a major source of global data on, for instance, mineral dust, which are needed for radiative and climate forcing assessments. Lidar remote sensing provides fast, reliable and unique vertical profiles of particles backscattering, such as mineral dust, under in-situ atmospheric conditions of temperature and humidity. There, the highly irregular shape of mineral dust particles is accounted for by carefully analyzing the polarization state of the electromagnetic radiation, allowing to evaluate the linear depolarization ratio, after robust calibration of the polarization detector (David et al. 2012; Miffre et al. 2019a). Hence, if a sufficiently high sensitivity is achieved on the polarization lidar detector, the complex vertical layering of mineral dust can be revealed in the free troposphere, even when mineral dust are involved in two or three component particle external mixtures, as we published (David et al. 2013; Mehri et al. 2018). However, the downside of such field measurements is that mineral dust particles cannot be identified with a sole polarization lidar backscattering experiment, as the measured depolarization is not mineral dust particles specific but dedicated to particles mixtures. In this context, controlled laboratory measurements are interesting as they allow studying the backscattering property of a determined ensemble of mineral dust particles, which may provide accurate inputs to better constrain lidar inversions.

1.3 Theoretical Considerations

We here consider elastic light backscattering at wavelength λ by an ensemble of particles with complex refractive index *m*, which are not static but move in an unbounded host medium such as ambient air. To describe the interaction of light with such a particles ensemble, the traditional approach is to approximate the particles ensemble as a macroscopic body on which the Maxwell's equations can be solved, hence ignoring the discreteness of matter, which avoids studying underlying quantum effects (Mishchenko et al. 2002). Under these assumptions, the backscattered electromagnetic field is a function of the free space dyadic Green function and the scatterer is perceived as a unique object with a spatial distribution of its complex refractive index *m*. In the far-field approximation, the simpler expression of the Green function leads to a simplified expression of the scattered electric field, then linked to the incident electric field through the amplitude scattering matrix (Mishchenko 2009).

(a) **Scattering matrix at near and exact backscattering angles**

To describe light backscattering by atmospheric non-spherical particles in laboratory, numerically or in field, the framework is hence that of the scattering matrix $[\boldsymbol{F}_\lambda]$, relating the incident and backscattered Stokes vectors $(St) = [I, Q, U, V]^{\mathrm{T}}$ which describe the polarization state of the incident and scattered light (Bohren and Huffman 1983):

$$\begin{pmatrix} I \\ Q \\ U \\ V \end{pmatrix} = \frac{1}{k^2 d^2}[F_\lambda(\theta)]\begin{pmatrix} I_i \\ Q_i \\ U_i \\ V_i \end{pmatrix} \tag{1}$$

where d is the distance from the particles ensemble to the detector and the i-subscript refers to the incident electromagnetic radiation. The first Stokes component I corresponds to the light intensity, Q and U describe linear polarization, while V accounts for circular polarization. The geometry is fixed by the scattering angle $\theta = (\boldsymbol{k}_0, \boldsymbol{k})$ where $k_0 = k = 2\pi/\lambda$ is the wave vector of the radiation. These wave-vectors define the scattering plane, used as a reference plane for defining the Stokes vectors of both incident and backscattered waves. In what follows, the scattering angle is equal to the lidar π –backscattering angle ($\theta = \pi$, i.e. exact backscattering angle). Near backscattering angles (i.e. $\theta < \pi$) are also considered in complement for the discussion. Under the far-field single scattering approximation (Mishchenko 2009), assuming particles in randomly-oriented, when particles present a plane of symmetry and / or when particles and their mirror particles are present in equal number, the scattering matrix $[\boldsymbol{F}_\lambda(\theta)]$ simplifies to a block-diagonal matrix:

$$[F_\lambda(\theta)] = \begin{bmatrix} F_{11}^\lambda(\theta) & F_{12}^\lambda(\theta) & 0 & 0 \\ F_{12}^\lambda(\theta) & F_{22}^\lambda(\theta) & 0 & 0 \\ 0 & 0 & F_{33}^\lambda(\theta) & F_{34}^\lambda(\theta) \\ 0 & 0 & -F_{34}^\lambda(\theta) & F_{44}^\lambda(\theta) \end{bmatrix} \tag{2}$$

The dimensionless scattering matrix elements $F_{ij}^\lambda(\theta)$ depend on θ and λ (noted as a superscript) but also on the particles size, shape and chemical composition, through their complex refractive index. At specific lidar exact π –backscattering angle ($\theta = \pi$), and as detailed by (van de Hulst 1957), $F_{33,d}^\lambda(\pi) = -F_{22,d}^\lambda(\pi)$ and $F_{12,d}^\lambda(\pi) = F_{34,d}^\lambda(\pi) = 0$ while application of the backscattering theorem leads to $F_{44}(\pi) = F_{11}(\pi) - 2F_{22}(\pi)$. Hence, the scattering matrix $[\boldsymbol{F}_\lambda(\pi)]$ reduces to only two non-vanishing elements $F_{11,d}^\lambda(\pi)$ and $F_{22,d}^\lambda(\pi)$:

$$[F_\lambda(\pi)] = \begin{bmatrix} F_{11}^\lambda(\pi) & 0 & 0 & 0 \\ 0 & F_{22}^\lambda(\pi) & 0 & 0 \\ 0 & 0 & -F_{22}^\lambda(\pi) & 0 \\ 0 & 0 & 0 & F_{11}^\lambda(\pi) - 2F_{22}^\lambda(\pi) \end{bmatrix} \tag{3}$$

Moreover, for spheres, $F_{22}(\theta) = F_{11}(\theta)$ and $F_{33}(\theta) = F_{44}(\theta)$ whatever the scattering angle [39] so that $F_{22}(\theta) = F_{11}(\theta)$ and $F_{33}(\theta) = F_{44}(\theta)$. Hence, for spheres at backscattering angle, $F_{22}(\pi) = -F_{33}(\pi) = -F_{44}(\pi) = F_{11}(\pi)$.

(b) Particles depolarization ratio at near and exact backscattering angles

At scattering angle θ and wavelength λ, the expression of the so-called particles depolarization ratio, hereafter briefly noted *PDR*, can be found in light scattering textbooks (Bohren and Huffman 1983; Mishchenko et al. 2002):

$$PDR(\lambda, \theta) = \frac{I - Q}{I + Q} = \frac{1 - F_{22}^\lambda(\theta)/F_{11}^\lambda(\theta)}{1 \pm 2F_{12}^\lambda(\theta)/F_{11}^\lambda(\theta) + F_{22}^\lambda(\theta)/F_{11}^\lambda(\theta)} \tag{4}$$

where the positive (resp. negative) sign corresponds to p-polarized (resp. s-polarized) incident electromagnetic radiation. As for the $F_{22}^\lambda(\pi)/F_{11}^\lambda(\pi)$-ratio, the particles depolarization *PDR* is an intrinsic property of the ensemble of non-spherical particles, which is mainly governed by the particles shape (Mishchenko et al. 2002). However, many other subtle effects such as particles inhomogeneity (Kahnert 2015; Liu et al. 2014) or surface roughness (Kemppinen et al. 2015) may play a role. For F_{11}^λ, F_{12}^λ and F_{22}^λ vary with the scattering angle θ depending on the size, the shape and the complex refractive index of the considered particles, so does the corresponding*PDR*. Therefore, the *PDR* at near backscattering angles ($\theta < \pi$) differs from that obtained at specific exact backscattering angle ($\theta = \pi$) at which lidar instruments operate as F_{11}^λ, F_{12}^λ and F_{22}^λ at near backscattering angles ($\theta < \pi$) may differ from their value at exact backscattering angle ($\theta = \pi$). The deviation of F_{11}^λ, F_{12}^λ and F_{22}^λ from their value at exact backscattering angle cannot be quantified because there is no analytical theory for light scattering by complex-shaped non-spherical particles such as mineral dust. Even if other existing light scattering laboratory experiments are approaching the specific π-angle very closely, close to the exact backward scattering direction, optical properties (and hence F_{11}^{λ}, F_{12}^{λ} and F_{22}^{λ}) may strongly vary as underscored in Mishchenko et al. (2002), so that accurate determinations of the particles depolarization, which are suitable for inverting remote sensing data and improving our fundamental knowledge of the backscattering process, can only be addressed at the specific π-angle. In this context, accurate laboratory evaluations of the dust lidar *PDR* are coveted and can only arise om laboratory experiments at lidar exact backscattering angle ($\theta = \pi$), for which Eq. (4) becomes:

$$PDR(\lambda, \pi) = \frac{I - Q}{I + Q} = \frac{1 - F_{22}^{\lambda}(\pi)/F_{11}^{\lambda}(\pi)}{1 + F_{22}^{\lambda}(\pi)/F_{11}^{\lambda}(\pi)} \tag{5}$$

Where the dependence of the dust lidar *PDR* with the π–backscattering angle has been omitted to ease the reading. In the lidar literature, the *PDR* is often also noted δ. Here, we will keep the *PDR* abbreviation for clarity. Following Eq. (5), to carry out accurate evaluations of the lidar *PDR*, the ratio $F_{22}^{\lambda}(\pi)/F_{11}^{\lambda}(\pi)$ must be precisely determined and $PDR(\lambda, \pi)$ should be clearly distinguished from its value at near backscattering $PDR(\lambda, \theta)$. In the literature, numerical extrapolations up to the π–backscattering angle exist (Gómez Martín et al. 2021; Liu et al. 2003) but we should wary of such extrapolations which are based on simplifying assumptions, which should be carefully checked. For that, laboratory experiments at exact backscattering angle are coveted.

1.4 State of the Art on LightBackscattering

The literature on light backscattering by atmospheric particles is abundant with field and laboratory experiments, completed with numerical simulations. To our knowledge, there is however a dearth of laboratory experiments to which this book chapter contributes to fill. We here recall the main contributions at near and exact backscattering angles.

(a) **Light backscattering numerical simulations**

To face such a complexity in size and shape, light-scattering numerical models have been developed which are becoming more and more realistic, with improved accuracies allowing an evaluation of the influence of the particles inhomogeneity (Kahnert 2015; Liu et al. 2014) and surface roughness (Kemppinen et al. 2015) on the scattering matrix elements. Such numerical simulations are now currently performed over the whole scattering angle range, hence including the exact backward scattering direction $\theta = \pi$. The literature on light backscattering numerical simulations is abundant (see http://www.scattport.org). Hence, the goal of this small paragraph is not to give an extensive overview of this important research field. To quote only a few reference examples on the case study of mineral dust, (Dubovik et al. 2006a) revealed the importance of the mathematical spheroidal model for accurate modelling of light scattering properties of complex-shaped particles such as mineral dust. The spheroidal model was tested by Müller et al. (2013) during the SAMUM field campaign. Using the spheroidal shape model for mineral dust during the SAMUM field campaign, (Müller et al. 2013) retrieved vertical profiles of microphysical properties by combining mineral dust polarization lidar with sun photometer measurements, and compared their results to airborne in situ observations. However, as underlined by Veselovskii et al. (2016), "*we should keep in mind that the spheroidal model was not specifically designed for lidar applications where scattering in the backward direction was considered*". Indeed, (Zubko et al. 2013) found that spheroids appeared to be inadequate for describing the dust particles' spectral dependence of linear polarization, while (Kemppinen et al. 2015) reported on difficulties in using ellipsoids to correctly retrieve dust particle properties from scattering data. The discrete-dipole approximation (DDA) numerical code was applied by Gasteiger et al. (2011) as another approach to compute light-scattering properties of mineral dust, though computationally demanding. In complement, (Kahnert et al. 2020) recently reviewed the size-dependence of the dust lidar *PDR* with a homogeneous spheroidal model, and also studied the dependence of the dust lidar *PDR* with the hematite volume fraction (Kahnert 2015). Recently, (Huang et al. 2020) revealed the importance of the dust complex refractive index for the development of a model of dust optical properties. Also, (Saito et al. 2021) developed a database of the optical properties of irregular aerosol particles for applications to radiative transfer simulations involving aerosols, particularly dust and volcanic ash particles. However, as underscored in (Haarig et al. 2022), complex particle shape models (Gasteiger et al. 2011; Mehri et al. 2018; Saito et al. 2021) are computationally expensive. The field of coherent backscattering was likewise studied by Videen and Muinonen (2015) who examined the evolution of light-scattering properties as a volume of particles increases from wavelength-sized to several hundreds of wavelengths, using the radiative-transfer coherent backscattering (RT–CB) model. Care should however be taken as no analytical solution to the Maxwell's equations exists for complex-shaped mineral dust so that these light scattering numerical simulations rely on simplifying assumptions that should be carefully checked. Hence, for these clear major advances to be fully beneficial, the underlying assumptions inherent to these numerical simulations should be carefully validated and for that controlled laboratory experiments are coveted, to in turn help developing even more accurate light-scattering models.

(b) Light backscattering in field: lidar remote sensing experiments

The lidar*PDR*, as retrieved from lidar remote sensing instruments, is commonly used to discriminate between low (rather spherical aerosol) and highly depolarizing particles (as mineral dust, (David 2013; David et al. 2013). The lidar *PDR* is also a crucial input for the CALIOP VFM production and categorization of aerosol subtype. As for above numerical simulations, the literature on lidar field measurements is really abundant and we here limit to some specific case studies, to which our group contributes (David et al. 2013; Mehri 2018; Miffre et al. 2012, 2019a, 2020). Moreover, in complex particle mixtures, the spectral behavior of the *PDR* can provide additional information on the plume composition (Haarig et al. 2018) and help to better constrain lidar inversions. As a result, for accurate assessments of aerosol microphysical properties, the accuracy on the retrieved lidar *PDR* is critical. Future lidar missions with UV (EarthCare) or spectral (AOS) depolarization capabilities will enhance our understanding of such mixing and its impact on climate and air quality, in areas where scarce ground-based observations are often available. However, to successfully retrieve the microphysical properties of for instance, mineral dust particles from such polarization lidar measurements, a robust inversion algorithm is required and for this, accurate input parameters are needed, at least to avoid confusions between mineral dust, sea-salt particles and other non-spherical particles. Hence, a precise knowledge of the mineral dust particles depolarization or dust *PDR* is required.

Several lidar field campaigns have hence been performed on mineral dust (Ansmann et al. 2011), studying the spectral dependence of *PDR* for dust as underscored by Burton et al. (2016) or Haarig et al. (2018). Recently, (Hofer et al. 2020) studied the optical properties of Central Asian aerosol for space borne lidar applications and aerosol typing at 355 and 532 nm. Likewise, (Haarig et al. 2022) provided the first triple triple-wavelength lidar observations of depolarization and extinction-to-backscatter ratios of Saharan dust. There, these authors finally underscored that "*it would be helpful—and a good addition to field observations – if laboratory measurements of the depolarization (…) in the 180_ backscatter direction could be realized for well-defined size fractions of real dust particles.*" A remaining issue is then to study the variation of the lidar *PDR* as a function of the particles size (close to the source, after long-range transport) and as a function of the particles origin or mineralogyx.

(iii) Light backscattering in laboratory

Starting from pioneering work by Hunt (1973), Liou and Lahore (1974) and Perry et al. (1978), light scattering by particles embedded in laboratory ambient air has been largely studied in laboratory with increased accuracies and accessible scattering angle ranges, as gathered in Table 1 at near ($\theta < \pi$) and exact backscattering angles ($\theta = \pi$). Apart from the accessible scattering angle range, the existing laboratory experimental set-ups differ from one another from the wavelength of the radiation, the studied samples and the nature of the laser source (CW, pulsed). Also, from a detailed reading of the corresponding papers, it seems difficult to know if the far-field single scattering conditions are fulfilled.

Light backscattering has been observed and applied however only on dense media such as solid GaAs crystals (Wiersma et al. 1997), biological tissues (Vitkin and Studinski 2001), or PSL spheres in liquid water (Kuga and Ishimaru 1984), or liquid animal blood (Wang et al. 2012). However, up to now to our knowledge, no laboratory experiment exists that covers the exact backward scattering direction for particles embedded in an unbounded host medium such as ambient air. As underscored by Huang et al. (2015), "*the phase matrix can be obtained only at specific wavelengths and in limited angular scattering regions, for example, from 3° to 177°*". Hence, the

Table 1 Existing laboratory light scattering experimental set-up for particles in air at near ($\theta < \pi$) and exact backscattering angles ($\theta = \pi$). To our knowledge, no laboratory experimental set-up exists addressing light scattering by aerosols at the specific lidar exact π–backscattering angle ($\theta = \pi$)

Sample	θ (°)	λ (nm)	Reference
Single dust particle	168.0–176.0	680	(Glen and Brooks 2013)
Ash, dust, water, NaCl	3–177	488, 520, 647	(Muñoz and Hovenier 2011)
Ice crystals Mineral dust	178.2	488	(Järvinen et al. 2016; Schnaiter et al. 2012)
Aerosol	0.3–177.6	532	(Gautam et al. 2020)
NaCl, water	179.2	532	(Sakai et al. 2010)
Mineral dust, water, pollen	176.0–180.0, 178	355 532	(Miffre et al. 2016, 2019b, 2022), Cholleton et al. (2020, 2022)

lack of experimental data in the backward direction limits the direct applicability of the measured scattering matrix elements for radiative transfer calculations. In particular, the absolute dependence on the F_{11}-element and hence the scattering phase function, remains unknown. The measured phase function is then normalized to unity at a particular scattering angle, chosen equal to 30° (Dabrowska et al. 2013; Liu et al. 2003; Volten et al. 2001).

In the absence of laboratory backscattering measurements, extrapolations have been performed to obtain data over the entire scattering angle range from 0° to 180°, as required for accurate radiative transfer calculations. To cover the exact backward scattering direction, polynomial extrapolations have then been proposed (Laan et al. 2009; Muñoz and Hovenier 2011; Volten et al. 2001). Videen et al. (2018) discussed on the interpolation of light scattering responses from irregularly-shaped particles and noted that the greatest discrepancy between the experiment and the modelled data occurs in the backscatter region. Though a synthetic scattering matrix has built (Laan et al. 2009), the added data points are somewhat artificial and the assumptions inherent to these extrapolations should be carefully checked, as analyzed by Liu et al. (2003) and more recently by (Huang et al. 2015). This requires to increase the accessible range of laboratory light scattering experiments to cover the gap from 177° up the π-backscattering angle with a high angular resolution (better than 1°). Hence, measurements of the scattering matrix at very large scattering angles are coveted.

Ideally, such a laboratory backscattering experiment should be conducted at several wavelengths, under the far-field single scattering approximation (Michael I Mishchenko et al. 2004a, b), to ease the comparison with numerical models (Dubovik et al. 2006a; Zubko et al. 2013). The Fig. 1 from Tesche et al. (2019) summarizes the state-of-the knowledge on the evaluation of the lidar *PDR* at backscattering angle as retrieved from field measurements, numerical simulations and laboratory experiments: while field measurements and numerical simulations are numerous, the dearth of laboratory *PDR* measurements at exact lidar backscattering angle ($\theta = \pi$)

is clearly underscored. Likewise, a laboratory approach is necessary to circumvent particles backscattering to a specific aerosol type instead of considering that of particle mixtures, which a priori differs (Miffre et al. 2011).

1.5 Outline of this Book Chapter

The goal of this book chapter is to present the current state-of-the-art on light backscattering by atmospheric particles. On account of the above considerations and to face the need for controlled laboratory experiments at exact backscattering angle, this book chapter mainly focuses on controlled laboratory experiments at near ($\theta < \pi$) and exact ($\theta = \pi$) backscattering angles for particles embedded in ambient air. These laboratory measurements of lidar *PDR* can help to better constrain future lidar inversions, but for that fundamental laboratory intensive work is required to address the dependence of the lidar *PDR* with size and mineralogy at lidar observation wavelengths (mostly 355 and 532 nm). Section 2 is then dedicated to a controlled-laboratory experiment at near backscattering angles (Miffre et al. 2019b). There, to complement existing laboratory light scattering experimental set-ups, the scattering matrix elements $F_{ij}^{\lambda}/F_{11}^{\lambda}(\theta)$ from 176.0° to backscattering angle with a 0.4° angular step for mineral dust. The ability of the mathematical spheroidal model to mimic light scattering by mineral dust at near backscattering angles is then verified. Section 3 is then specifically dedicated to the cutting-edge laboratory π-polarimeter at exact backscattering angle or lidar angle ($\theta = \pi$), with emphasis on its ability to accurately measure the backscattered light intensity and the corresponding lidar*PDR*. This laboratory π-polarimeter is important to interpret lidar observations, which operate at strict backscattering angle $\theta = \pi$. Several case studies are then presented on laboratory light backscattering by:

- *Spherical inorganic sulfates,* for sulfates are responsible for a net cooling of the Earth's atmosphere due to their ability to backscatter light, and also as a way to validate the laboratory π-polarimeter as light backscattering by spherical sulfates follow the Lorenz-Mie theory.
- *Core–shell organic sulfates,* for the sulfate aerosol may give rise to core–shell structures in the presence of organic compounds in the atmosphere. The question is there to quantify the modification of the sulfates ability to backscatter light (Dubois et al. 2021).
- *Freshly-emitted soot,* as black carbon is the second contributor to global warming after CO_2 and a major absorber of solar radiation (Stier et al. 2007). Additionally, the carbon aerosol has a strong impact on human health, especially in urban polluted areas, as being carcinogenic. Moreover, understanding light backscattering by soot particles is essential for radiative transfer, as well as to develop carbon reduction emission strategies. In the literature, the soot lidar *PDR* has

been the subject of several publications, from light scattering numerical simulations at backscattering, but also from lidar field experiments in plumes. The proposed controlled-laboratory experiment complements these publications.

- *Mineral dust,* for it is one of the major contributors to the Earth's global aerosol load, with emission rates as large as 1000 to 3000 $\mathrm{Tg.yr^{-1}}$ from the Earth's surface (Monge et al. 2012). This abundant aerosol is uplifted into the atmosphere through favorable winds and can be transported by advection over several thousands of kilometers, hence affecting the Earth's climate at both local, regional and global scales. The radiative properties of mineral dust are however difficult to handle mainly due to the complexity in shape of these particles, which are highly irregularly-shaped, with sharp edges and sometimes even surface roughness. Hence, the dust particles non-sphericity is still a major issue for accurate radiative forcing assessments (Mehri et al. 2018). The intrinsic lidar *PDR* of mineral dust is analyzed for several dust samples differing in sizes and mineralogy by taking benefit from the laboratory π-polarimeter at exact backscattering angle (Miffre et al. 2016, 2019b, 2022).

Implications of this laboratory work on aerosols light backscattering in lidar remote sensing experiments are proposed and discussed in Sect. 4. The chapter ends with a conclusion and proposes outlooks.

2 Light Scattering at Near Backscattering Angles ($\theta < \pi$)

2.1 The Laboratory $\pi+\varepsilon$ Polarimeter

The laboratory π+ε-polarimeter is schemed in Fig. 1 from Miffre et al. (2019b). To evaluate the ratios $F_{ij}^{\lambda}/F_{11}^{\lambda}(\theta)$ of the scattering matrix elements at near backscattering angles ($\theta < \pi$) and wavelength λ for particles in ambient air, light scattering measurements are carried out for a set of incident polarization states, namely $(p, 45+, RC)$, as explained below. The scattering angle is varied from 176.0° up to 180.0° with 0.4° angular resolution by modifying the wave-vector $\boldsymbol{k_i}$ of the incident radiation by 0.2° steps, which in turn varies the scattering angle $\theta = (\boldsymbol{k_i}, \boldsymbol{k_s})$, while $\boldsymbol{k_s}$ is the wave-vector of the backscattered radiation. The light detector is identical to that used in the exact backward scattering experimental set-up to be described in the paragraph below. In this way, the same light detector is used for evaluating the scattering matrix ratios $F_{ij}/F_{11}(\theta)$ at both near ($\theta < \pi$) and exact ($\theta = \pi$) backscattering angles, which minimizes biases in the $F_{ij}/F_{11}(\theta)$-evaluation.

2.2 Scattering Matrix Elements Retrieval at Near Backscattering ($\theta < \pi$)

Basically, the Stokes vectors (St_i) and (St) of the incident and backscattered radiations relate with the Mueller matrix $\left[\boldsymbol{M}_{\boldsymbol{\theta}}^{\boldsymbol{\lambda}}\right]$ of the π(+ε)-polarimeter at scattering angle θ and wavelength λ as follows $(St) = \left[\boldsymbol{M}_{\boldsymbol{\theta}}^{\boldsymbol{\lambda}}\right](St_i)$. $\left[\boldsymbol{M}_{\boldsymbol{\theta}}^{\boldsymbol{\lambda}}\right]$ can be obtained by taking into account the successive Mueller matrices encountered by the laser pulse from the laser source to the particles then back to the light detector. Following Fig. 3, the Mueller matrix of the set-up is equal to $[\mathbf{PBC}][\mathbf{QWP}][\boldsymbol{F}_{\boldsymbol{\lambda}}(\theta)]$ where $[\boldsymbol{F}_{\boldsymbol{\lambda}}(\theta)]$ is the scattering matrix at scattering angle θ and wavelength λ as given in Eq. (2) for $\theta < \pi$ and in Eq. (3) for $\theta = \pi$. At scattering angle θ and wavelength λ, the detected scattered intensity is then given by the first component of (St):

$$I_\theta^\lambda = \frac{\eta_\lambda P_{0,\lambda}}{d^2}(P_j)[\mathbf{PBC}][\mathbf{QWP}][\boldsymbol{F}_{\boldsymbol{\lambda}}(\theta)](St_i) \tag{6}$$

where η_λ is the electro-optics efficiency of the detector at wavelength λ, $P_{0,\lambda}$ is the incident laser power and $(P_j) = [1, 0, 0, 0]$ is a projection unitary raw vector. In this book chapter, we will mainly focus on exact backscattering ($\theta = \pi$) of light by particles in line of the motivations presented in Sect. 1.4 for studying exact light backscattering and noticeably for lidar purposes. Readers interested by retrieving the scattering matrix elements $F_{ij}^\lambda/F_{11}^\lambda(\theta)$ at near backscattering angles ($\theta < \pi$) by using the laboratory π+ε-polarimeter can refer to Miffre et al. (2019b) where the methodology is extensively described and where the calculus are detailed. We here only briefly present the outputs of these calculations for completeness. Following (Miffre et al. 2019b), the detected scattered intensity can then be written as follows:

$$I_\theta^\lambda(\psi) = I_{11}^\lambda(\theta) \times \left[a_\theta^\lambda - b_\theta^\lambda \sin(2\psi) - c_\theta^\lambda \cos(4\psi) - d_\theta^\lambda \sin(4\psi)\right] \quad \text{for } \theta < \pi \tag{7}$$

where the superscript refers to the wavelength of the radiation while the coefficients a_θ^λ to d_θ^λ are given in Table 2 for incident polarization states (p, 45+, RC). $I_{11}^\lambda = \eta_\lambda P_{0,\lambda} F_{11}^\lambda/(4d^2)$ is the detected scattered phase function, as being proportional to

Table 2 Expression of the coefficients the a_θ to d_θ appearing in the expression of the scattered light intensity in Eq. (11) as a function of the scattering matrix elements $f_{ij}^\lambda(\theta) = F_{ij}^\lambda/F_{11}^\lambda(\theta)$ for incident polarization states (p, 45+, RC). The dependence of f_{ij} with scattering angle θ has been omitted to ease the reading

State	(St_i)	a_θ^λ	b_θ^λ	c_θ^λ	d_θ^λ
p	$[1, 1, 0, 0]^T$	$2 - f_{22} + f_{12}^\lambda$	0	$f_{12}^\lambda + f_{22}$	0
45+	$[1, 0, 1, 0]^T$	$2 - f_{12}^\lambda$	$2f_{34}^\lambda$	f_{12}^λ	f_{33}^λ
RC	$[1, 0, 0, 1]^T$	$2 - f_{12}^\lambda$	$-2f_{44}^\lambda$	f_{12}^λ	f_{34}^λ

F_{11}^{λ}. To ease the reading, we will use the following reduced notation $f_{ij}^{\lambda} = F_{ij}^{\lambda}/F_{11}^{\lambda}$. From Table 2, it is clear that the scattering matrix elements at $\theta < \pi$ can then be retrieved as follows:

$$f_{33}^{\lambda}(\theta) = 2d_{\theta,45+}^{\lambda}/(a_{\theta,45+}^{\lambda} + c_{\theta,45+}^{\lambda}) \tag{8a}$$

$$f_{44}^{\lambda}(\theta) = -b_{\theta,RC}^{\lambda}/(a_{\theta,45+}^{\lambda} + c_{\theta,45+}^{\lambda}) \tag{8b}$$

$$f_{12}^{\lambda}(\theta) = 2c_{\theta,RC}^{\lambda}/(a_{\theta,45+}^{\lambda} + c_{\theta,45+}^{\lambda}) \tag{8c}$$

$$f_{34}^{\lambda}(\theta) = 2d_{\theta,RC}^{\lambda}/(a_{\theta,45+}^{\lambda} + c_{\theta,45+}^{\lambda}) \tag{8d}$$

$$f_{22}^{\lambda} = [f_{12}^{\lambda}(\theta) \cdot \left(c_{\theta,p}^{\lambda} - a_{\theta,p}^{\lambda}\right) + 2c_{\theta,p}^{\lambda}]/\left(a_{\theta,p}^{\lambda} + c_{\theta,p}^{\lambda}\right) \tag{8e}$$

where subscripts (p, 45+, RC) respectively refer to considered (p, 45+, RC) incident polarization states. From a practical point of view, the coefficients a_{θ}^{λ} to d_{θ}^{λ} are retrieved by adjusting the $I_{\theta}^{\lambda}(\psi)$-variations with Eq. (7). To gain in accuracy in the $f_{ij}^{\lambda}(\theta)$-evaluation, the backscattered light intensity is measured for different positions of the QWP, over a complete rotation of QWP (ψ-modulation angle).

The scattered intensity $I_{\theta}(\psi)$ for incident polarization (p) exhibits several minima equal to $1 - f_{22}^{\lambda}$, to be related to particles deviation from isotropy or linear depolarization. The sensitivity of $I_{\theta}(\psi)$ to a modification in f_{33}^{λ} and f_{34}^{λ} is seen with incident polarization(45+), which exhibit different secondary maxima and minima. The sensitivity of $I_{\theta}(\psi)$ to f_{44}^{λ} is seen with incident polarization(RC), where the minima are equal to $1 + f_{44}^{\lambda}$ and related to circular depolarization. These latter minima are not null, even for spherical particles, since f_{44}^{λ} only equals unity at exact backscattering angle, as explained in Sect. 1.3.

2.3 Light Scattering by Mineral Dust at Near Backscattering Angles ($\theta < \pi$)

In Fig. 6 from Miffre et al. (2019b) are plotted the variations of the light intensity $I_{\theta}^{\lambda}(\psi)$ scattered by the generated ATD-particles at scattering angles $\theta = 176.0°$ and $\theta = 178.0°$ for incident polarization states (p, 45+, RC) at 532 nm wavelength. The observed variations of $I_{\theta}^{\lambda}(\psi)$ are representative of a determined size and shape distribution of the generated mineral dust particles: if the size of the dust sample was varying, the variations of $I_{\theta}^{\lambda}(\psi)$ would not exhibit constant maxima while rotating the QWP. Likewise, the shape distribution of the dust particles did not vary during the acquisitions, otherwise, $I_{\theta}^{\lambda}(\psi)$ would exhibit varying minima (recall: these minima are related to particles non-sphericity, as being equal to$1 - f_{22}^{\lambda}$). It is hence clear that mineral dust are non-spherical particles since the minima of $I_{\theta}(\psi)$ are not null, at both scattering angles. As a result,$f_{22}^{\lambda}(\theta)$ differs from unity. Also, the minima, equal to$1 + f_{44}^{\lambda}$, are far from zero, as a clear signature of circular depolarization of the generated mineral dust particles. By adjusting these experimental data points with Eq. (11), the coefficients a_{θ}^{λ} to d_{θ}^{λ} can be retrieved for each scattering angle to precisely evaluate the ratios$f_{ij}^{\lambda}(\theta)$ of scattering matrix elements by applying Eq. (7), as given in Fig. 7 from Miffre et al. (2019b). Within our experimental error bars, we conclude that$f_{22}^{\lambda}(\theta) < 1$ and $f_{33}^{\lambda}(\theta)$ differs from $f_{44}^{\lambda}(\theta)$ at all scattering angles as optical signatures of linear and circular depolarization from mineral dust. At exact backscattering angle, we evaluate$f_{22}^{\lambda}(\pi) = 0.57 \pm 0.02$ shows that$f_{44}^{\lambda}(\theta)$ tends towards $1 - 2f_{22}^{\lambda}(\pi) = -0.14$, as expected when approaching the exact backward scattering angle. Likewise,$f_{33}^{\lambda}(\theta)$ tends towards$-f_{22}^{\lambda}(\pi) = -0.57$, as expected. With the generated size distribution of mineral dust to be seen in Fig. 6(f), the scattering matrix elements slightly vary in the scattering angle range between 176.0° and 180.0°, but this should not be considered as a general establish fact for mineral dust may present different size, shape distributions and mineralogy leading to other light scattering properties. This is especially true close to the backscattering angle where optical properties may strongly vary. Hence, to draw such a conclusion, complementary studies should be carried out. Section 3.6 starts tackling this important issue.

2.4 Comparison with T-matrix Numerical Simulations

As the laboratory π+ε-polarimeter operates in the far-field single scattering approximation, the ability of the mathematical spheroidal model to mimic light backscattering can be discussed by comparison with our laboratory findings. This work hence extends the conclusions by Dubovik et al. (2006b) up to the backward scattering direction. Though the highly irregular shape of mineral dust is difficult to account for in mathematical models, we tested the applicability of the widely used spheroidal model, for the first time to our knowledge in the scattering angle range between 176.0° and 180.0°. For our laboratory π-polarimeter fulfills the far-field single-scattering approximation, the measured depolarization can be compared with the results from numerical simulations. In this section, we discuss the applicability of a spheroidal model for numerically simulating the dust particles scattering at near and exact backscattering angles. The T-matrix method (Mishchenko and Travis 1998), based on the spheroidal model, is an exact analytical solution of the Maxwell equations, allowing averaging over particle orientations. The T-matrix method is extensively described in the literature. In a few words, in the T-matrix method, the size-shape distribution of randomly-oriented mineral dust particles can be mimicked with size-shape distributions of spheroids, the simplest shape for non-spherical particles, with axial symmetry and a geometry described by the aspect ratio $\varepsilon = b/a$, where a and b are the major (minor) and minor (major) axis lengths for oblate (prolate) spheroids respectively. The aspect ratios were then distributed either as equiprobable ($f(\epsilon) = \varepsilon^n$ with $n = 0$) or with a $n = 3$ power-law shape distribution, in an attempt to better account for polarization effects (Merikallio et al. 2011). Using $m = 1.555 + 0.005i$ for the refractive index of ATD at $\lambda = 532$ nm [34], we then applied Mishchenko's T-matrix numerical code (Mishchenko and Travis 1998) to retrieve the ratios of scattering matrix elements after size-integration using Fig. 5(f). To derive the size distribution for non-spherical ATD-particles, we took benefit from recent publication by Chien et al. (2016), allowing to correlate optical diameters to aerodynamic diameters. More precisely, Eqs. (5) and (9) from Chien et al. (2016) were applied, using 1.5 for the shape factor for non-spherical ATD-particles, to convert the mobility diameters (from our SMPS) and the optical diameter (from our particle counter) to volume equivalent diameters, as plotted in Fig. 6(f). Our numerical results are presented in Fig. 6(a) to (e) in dashed lines for the $n = 3$ shape distribution and in dotted lines for the $n = 0$ shape distribution. Interestingly, within our experimental error bars, the output of T-matrix numerical simulation agrees with our laboratory findings for $f_{44}^{\lambda}(\theta), f_{12}^{\lambda}(\theta)$ and also for a majority of points for $f_{34}^{\lambda}(\theta)$ and $f_{22}^{\lambda}(\theta)$. The agreement is better when using the $n = 3$ shape distribution rather than the equiprobable shape distribution of spheroids, in agreement with [34], where we observed a similar behaviour at specific backscattering angle. This conclusion cannot however be supported by electron microscopic images, since as underscored by Kahnert et al. (2014): "“*single spheroids do not share the single-scattering properties of non-spheroidal particles with the same aspect ratios, so one should not think that when using spheroids to mimic scattering by more complex particles, best results would be achieved using aspect ratios of the target particles for the spheroids.*" A slight discrepancy of 0.06 is however observed for $f_{33}^{\lambda}(\theta)$ even with the $n = 3$ shape distribution.

We should however keep in mind that the uncertainty on the scattering angle is $\pm 0.2°$ and that the size distribution displayed in Fig. 7(f) from Miffre et al. (2019b) is not error-free. Also, the refractive index of ATD is itself not error-free: its calculation in Miffre et al. (2016) is based on the Aspens formula which requires prior knowledge of the refractive indices of each oxide present in ATD as well as their volume fractions. Interestingly, our laboratory evaluation of the scattering matrix elements agrees with that computed in the well-known paper by Dubovik et al. (2006b): at near and exact backscattering, his computed phase matrix elements were indeed equal to: $P_{12}/P_{11} \simeq 0$, $P_{22}/P_{11} \simeq 0.55$, $P_{33}/P_{11} \simeq -0.55$, $P_{34}/P_{11} \simeq 0$ and $P_{44}/P_{11} \simeq -0.15$. Care should however be taken since scattering matrix elements depend on the particles size distribution and refractive index.

3 Light Backscattering at Exact Backscattering Angle ($\theta = \pi$)

Addressing light backscattering by particles embedded in ambient air in laboratory is challenging as two main difficulties then arise:

- The first intricacy is relative to the finite size of the detector, which may block the incident radiation. The insertion of a beam splitter, as often performed for condensed matter phases usually limits the accuracy on the backscattering measurement as its specifications are imperfectly known and represent an important artifact, source of systematic error (Wiersma et al. 1997). Inserting a beam splitter plate also creates stray light affecting the particles backscattering signal, as for solid biological tissues (Studinski and Vitkin 2000).
- The second intricacy is relative to the intensity of the backscattered radiation itself, which might be weak for particles in air, especially for non-spherical particles for which backscattering is weaker (Kahnert et al. 2014). Hence, any stray light may overcome the particles backscattered radiation. For condensed matter phases, lock-in detection has been applied on continuous incident radiation (Studinski and Vitkin 2000; Vitkin and Studinski 2001), but for particles in ambient air, the particles backscattering signal is so weak that even this technique has not been successfully applied.

Hence, observing exact light backscattering ($\theta = \pi$) by atmospheric particles in laboratory requires a high angular resolution (to avoid blocking the incident light with the detector) and a high dynamical range (to discriminate the weak backscattered radiation from background stray light). In (Miffre et al. 2016, 2019b, 2022), for the first time to our knowledge, we overcame these two intricacies as detailed below in the so-called laboratory π-polarimeter. This π-polarimeter allows accurate retrievals of $F_{22}^{\lambda}/F_{11}^{\lambda}(\pi)$ and hence of the lidar *PDR*, without any extrapolation based on numerical simulations, which are actually performed in the literature (Gómez Martín et al. 2021; Liu et al. 2003).

3.1 The Laboratory π-polarimeter ($\theta = \pi$)

The laboratory π-polarimeter is a cutting-edge experiment, schemed in Fig. 1 from Miffre et al. (2016). It is actually composed two π-polarimeters, one per wavelength (see Fig. 3 from Miffre et al. (2016)), to allow addressing the spectral dependence of the lidar *PDR* at 355 and 532 nm wavelengths simultaneously, as often performed in lidar applications (Haarig et al. 2018, 2022). The exact backscattering geometry ($\theta = \pi$) is achieved by precisely aligning (1 mm out of 10 m) a retro-reflecting polarizing beam splitter cube (PBC) along the z-optical axis from a laser source to the particles scattering volume, to cover the lidar exact backscattering direction with accuracy: θ = (180.0±0.2)°. In the exact backward scattering direction, stray scattered light from optical components can be significant and to overcome this difficulty, the particles backscattering radiation is discriminated from background stray light by achieving time-resolved measurements synchronized with the laser pulse, to address the time-of-flight $2d/c$ taken by the laser pulse to reach the detector after the scattering event. Particles light backscattering can then be distinguished from that due to laboratory ambient air, by first recording the backscattered light intensity in the presence of the particles, then in their absence, to retrieve the particles backscattered light intensity I_{π}^{λ} by subtracting these latter two (David 2013). The experiment is carried out in laboratory ambient air: chamber walls and windows, with inherent AR-coatings, may indeed provoke a strong backscattering signal or/and modify the polarization of the backscattered radiation which has to be accurately analyzed. The particles are not static but move in a few millimeters wide beam, whose section is defined by the 2.5 mm diameter injection nozzle, chosen to fill the 8 cm^3 detected backscattering volume. Moreover, to ease the comparison with numerical simulations and field experiments, the laboratory π-polarimeter operates in the far-field single scattering approximation and efficiently collects the backscattered radiation, while minimizing any stray light, within a very small (3 mrad) field of view, as in lidar applications, to cover the exact backscattering direction with accuracy $\theta = (180.0\pm0.2)°$. The lidar *PDR* can then be evaluated from the ratio $F_{22}^{\lambda}/F_{11}^{\lambda}$ following the methodology described below (Miffre et al. 2016).

3.2 Scattering Matrix Elements and Lidar PDR Retrieval at Backscattering ($\theta = \pi$)

At exact backscattering angle ($\theta = \pi$), following Fig. 7, due to the co-axial geometry, the incident Stokes vector is determined by the combination of the PBC and the QWP and expresses as $(St_i) = \left[QWP\right][PBC][1, 1, 0, 0]^T = [1, \cos(2\psi) - \sin(4\psi)/2, -\sin(2\psi)]^T$. As detailed in Appendix A of (Miffre et al. 2019b), we hence get for the detected backscattered intensity:

$$I_{\pi}^{\lambda}(\psi) = I_{11}^{\lambda}(\pi) \times \left[a_{\pi}^{\lambda} - c_{\pi}^{\lambda}\cos(4\psi)\right] \tag{9}$$

where the coefficients a_{π}^{λ} and c_{π}^{λ} depend on the backscattering matrix elements at wavelength λ as follows: $2a_{\pi}^{\lambda} = 1 + F_{22}^{\lambda}/F_{11}^{\lambda}$ and $2c_{\pi}^{\lambda} = 3F_{22}^{\lambda}/F_{11}^{\lambda} - 1$. Hence, following Eq. (9), the $c_{\pi}^{\lambda}/a_{\pi}^{\lambda}$-ratio can be determined from the $I_{\pi}^{\lambda}(\psi)$-variations independently on $I_{11}^{\lambda}(\pi)$. As a result, $F_{22}^{\lambda}/F_{11}^{\lambda}(\pi)$ can be precisely evaluated from the c_{π}/a_{π}-ratio [34]:

$$F_{22}^{\lambda}/F_{11}^{\lambda}(\pi) = (1 + c_{\pi}^{\lambda}/a_{\pi}^{\lambda})/(3 - c_{\pi}^{\lambda}/a_{\pi}^{\lambda}) \tag{10}$$

As a result, accurate evaluations of the aerosol lidar *PDR* can then be retrieved as:

$$PDR_{\pi}^{\lambda} = \left(1 - c_{\pi}^{\lambda}/a_{\pi}^{\lambda}\right)/2 \qquad (11)$$

independently of $I_{11}^{\lambda}(\pi)$. Accordingly, the applied voltage to the UV and VIS-photodetectors will be adjusted to each particles sample to gain in accuracy in the retrieved lidar *PDR*. From a practical point of view, the coefficients a_{π}^{λ} and c_{π}^{λ} are retrieved by adjusting the $I_{\pi}^{\lambda}(\psi)$-variations with Eq. (11) to get accurate determinations of $I_{11}^{\lambda}(\pi) \times a_{\pi}$ and $I_{11}^{\lambda}(\pi) \times c_{\pi}$, then $c_{\pi}^{\lambda}/a_{\pi}^{\lambda}$ and the *PDR* from Eq. (11). To fix ideas, as long as the lidar *PDR* increases, the backscattered light intensity becomes weaker, in agreement with the literature (Kahnert et al. 2014). All curves exhibit non-vanishing minima as the observed minima are equal to$a_{\pi}^{\lambda} - c_{\pi}^{\lambda} = 1 - F_{22}^{\lambda}/F_{11}^{\lambda}$, which never cancels for nonspherical particles such as soot or mineral dust. These minima can be used as an indicator for particles' deviation from isotropy. The lidar *PDR* is however also determined by the curve maxima equal to $a_{\pi}^{\lambda} + c_{\pi}^{\lambda} = 2F_{22}^{\lambda}/F_{11}^{\lambda}$. Indeed, if $I_{\pi,m}^{\lambda}$ and $I_{\pi,M}^{\lambda}$ refer to the curve minimum and maximum, following Eq. (12), the lidar *PDR* can be retrieved from $I_{\pi,m}^{\lambda}/(I_{\pi,m}^{\lambda} + I_{\pi,M}^{\lambda})$, independently of I_{11}^{λ}.

Special care has been taken to precisely evaluate the uncertainties on the retrieved *PDR*. The systematic errors in the backscattering π-polarimeter are that encountered in 2λ-polarization lidar experiments (Freudenthaler et al. 2009; Haarig et al. 2022), which we extensively studied in a dedicated paper (David et al. 2012). In a few words, systematic errors then arise from:

- *Imperfect definition of the polarization state of the incident radiation.* In the π–polarimeter, the polarization state of the electromagnetic radiation emerging from the laser is precisely set to $[1, 1, 0, 0]^T$ (i.e. with no remaining ellipticity) by using two successive *PBC*.
- *Polarization cross-talks between the emitter and the detector polarization axes.* Likewise, on the detector side, to account for the imperfections of the retro-reflecting *PBC* ($R_s > 99.5\%, T_p > 90\%$), a secondary *PBC* is inserted between the retro-reflecting *PBC* and the light detector to ensure polarization cross-talk or undesired fraction R_pT_s originating from the p-component of the backscattered radiation to be fully negligible. Hence, the π–polarimeter is sensitive to the s-component of the backscattered radiation only. Also, the emitting *PBC* being used as retro-reflecting PBC, any possible mismatch between the s-polarization axis of the emitted and detected backscattered radiations cannot occur. Introducing controlled amounts of polarization cross-talks is however interesting to calibrate polarization lidars as explained in Sect. 4 and in Miffre et al. (2019a).
- *Wavelength cross-talks between the UV and the VIS-backscattered radiations.* Likewise, wavelength cross-talks are minimized by using selective interference filters exhibiting an optical density higher than 5 at 355 nm wavelength in the VIS π–polarimeter and at 532 nm wavelength in the UV π–polarimeter.
- *Multiple scattering may eventually occur and cause further light depolarization.* However, the single-scattering approximation (*SSA*) is rather safe in our laboratory backscattering experiment (Mishchenko et al. 2007) where the particles are moving in a thin (2.5 mm) wide beam so that the volume element is optically thin in contrary to atmospheric chambers.

3.3 Light Backscattering by Spherical Sulfates in Laboratory

Light backscattering by sulfate particles is extremely important as sulfates are responsible for a net cooling of the Earth's atmosphere due to their ability to backscatter light. Figure 4 from Miffre et al. (2016) displays the measured variations of $I_\pi^\lambda = f(\psi)$ at both UV and VIS wavelengths. Both curves exhibit zero minima, showing the zero-depolarization of spherical sulfate particles, in agreement with Lorenz-Mie theory. To be quantitative, we adjusted the UV and VIS curves and their respective successive minima and maxima by using Eqs. (3–5) to retrieve the F_{22}/F_{11} ratio:

$$\begin{aligned} F_{22}^\lambda/F_{11}^\lambda(sulfates, \lambda = 355\,nm) &= 0.9945 \pm 0.0065 \\ F_{22}^\lambda/F_{11}^\lambda(sulfates, \lambda = 532\,nm) &= 1.0037 \pm 0.0049 \end{aligned} \tag{12}$$

The precision on the F_{22}/F_{11} ratio is remarkable and results from the precision achieved in the laboratory π-polarimeter and on the stability of the particles generator. The corresponding *PDR* is then obtained by applying Eqs. (3–6):

$$\begin{aligned} PDR_\pi^\lambda(sulfates, \lambda = 355\,nm) &= (0.28 \pm 0.33)\% \\ PDR_\pi^\lambda(sulfates, \lambda = 532\,nm) &= (0.19 \pm 0.24)\% \end{aligned} \tag{13}$$

The observed zero depolarization is compatible with Lorenz-Mie theory, which in turn validates the ability of the laboratory π-polarimeter to accurately measure the lidar *PDR* of sulfates at both wavelengths. Although more than a century has now elapsed since G. Mie presented his theory (Mie 1908), even though measurements of water clouds do not contradict the Mie theory, it is surprising that its experimental proof had never been achieved in laboratory in the exact backscattering direction for aerosols, such as spherical water droplets or sulfate particles, while, in the literature, a considerable number of papers apply the Lorenz-Mie theory, as for environmental purposes, such as in remote sensing and radiative transfer applications.

3.4 Light Backscattering by Core–Shell Organic Sulfates in Laboratory

Conversely, the impact of organic aerosol on the Earth's radiative balance remains elusive as it is associated with large uncertainties. While it was assumed that sulfur is primarily present in its inorganic forms (e.g., SO_4^{2-}, HSO_4^-, HSO_3^-), field and laboratory studies (Riva et al. 2019; Shakya and Peltier 2013, 2015; Surratt et al. 2008; Tolocka and Turpin 2012) recently showed that organosulfur compounds, including organosulfates, are important contributors to the total sulfate aerosol mass. This paragraph summarizes the outputs of a cooperative work between our group and chemical colleagues (Dubois et al. 2021). There, we revealed an unexpected trend with a net decrease in light backscattering by the sulfate aerosol in the presence of organic compounds, giving rise to core–shell structures. These complex organic compounds (isoprene epoxydiols, IEPOX) or organosulfates are the most important secondary organic aerosol precursors in the atmosphere. This finding suggests that, when organic compounds, including organosulfates are present, the ability of inorganic sulfate particles to backscatter light is greatly decreased. Hence, our laboratory findings are key for quantifying the direct radiative forcing of sulfates in the presence of organic compounds, thus more clearly resolving the impact of such aerosol particles on the Earth's climate.

In more details, measuring the light backscattered by organic sulfates represented a real experimental challenge due to the very low backscattering cross-section of such particles presenting sizes in the hundreds of nanometers range only. However, the sensitivity achieved in the laboratory backscattering polarimeter was sufficiently high: using the laboratory π-polarimeter, controlled-laboratory experiments were performed to compare the backscattered light intensity by organic / inorganic sulfates. Figure 3 from Dubois et al. (2021) displays the corresponding backscattered light intensity $I_{\pi}^{\lambda} = f(\psi)$ at both UV and VIS-wavelengths. The curve minima being null, organic and inorganic sulfates remained spherical during the acquisition. The curve maxima $I_{\pi,M}^{\lambda}$ of $I_{\pi}^{\lambda} = f(\psi)$, which correspond to an incident s-polarized radiation, could then be used as a metrics of the backscattered light intensity (the π-polarimeter measures the s-polarization component of the backscattered radiation, which is preserved during the backscattering process for spherical particles). A precise evaluation of these maxima was then performed by adjusting our experimental data points with a $\cos(4\psi)$ curve.

The key point is that the $I_{\pi,M}^{\lambda}$ maxima were representative of a determined particles number density, size distribution and refractive index. Indeed, if the particles number density or size distribution had varied during the backscattering experiments, the maxima $I_{p,M}$ would not have remained constant when varying the wave-plates orientation. Likewise, potential variations in particle number concentrations when considering the conversion from inorganic to organic sulfates were accounted for by considering $I_{\pi,M}^{\lambda}/N_{tot}$ where N_{tot} is the integral of the particle number density over the particles size distribution (Dubois et al. 2021). Hence, the observed decrease can only be due to variations in the complex refractive index from inorganic to organic sulfates. To be quantitative, the experiment was then repeated for increased organic (IEPOX) gas phase concentrations to reveal a net decrease in the normalized backscattered light intensity $I_{\pi,M}^{\lambda}/N_{tot}$ of 16% at 532 nm wavelength and 12% at 355 nm wavelength from inorganic to organic sulfates.

We then compare our laboratory findings with the outputs given by Lorenz-Mie light scattering numerical simulations to compute the backscattering cross-section C_{back} (resp. $C_{back,0}$) of organic (resp. inorganic) particles using the particles size distributions measured for the sulfate and organics mixture. As a first step, C_{back} was computed for the refractive index of ammonium sulfate ($m = 1.445$) (Cotterell et al. 2017) and organics (IEPOX-derived secondary organics aerosols, $m = 1.43 + 0.002$j) (Nakayama et al. 2018). The observed decrease in C_{back} could not be reproduced by size effects only and was therefore related to variations in the complex refractive index. To account for the presence of both AAS and IEPOX-derived SOA compounds, we then applied effective medium theories, by applying the Aspens formula, providing the effective particles complex refractive index of a backscattering medium containing a mixture of AAS and IEPOX-derived SOA products. As displayed in Fig. 5 from Dubois et al. (2021) however, the variations of $C_{back}/C_{back,0}$ did not more faithfully reproduce our laboratory observations when considering AAS volume fractions in the AAS and IEPOX-derived SOA particle mixtures ranging from 0.96 to 1.00, with 0.02 step, consistent with performed chemical analyses. As a result, the effect on C_{back} of a possible change in the internal structure of the particles was investigated. Indeed, the reactive uptake of IEPOX is known to produce core–shell structures.(Olson et al. 2019; Riva et al. 2019; Zhang et al. 2018) To investigate the case of a stratified dielectric sphere (i.e., a spherical inorganic core coated by a spherical organic shell), we applied the numerical code from (Ackerman and Toon 1981) an extension of the Lorenz-Mie theory, suitable for thin film absorbent particles as was expected in our experiments. When adjusting the core/shell radius to consider the above volume fractions, we reproduced a part of the observed decrease inC_{back}. Considering an IEPOX refractive index of $1.43 + 0.5j$ led to a decrease in the backscattering cross-section$C_{back}/C_{back,0}$ by about 18% at 532 nm wavelength (see Fig. 5 from (Dubois et al. 2021)), in the same range as that observed in laboratory. Hence, the formation of an inorganic core organic shell structure can be key for explaining the reported decrease, though effective medium theories may also be key.

3.5 Light Backscattering by Soot Particles in Laboratory

Likewise, the laboratory π-polarimeter has been used to quantify the lidar *PDR* of freshly emitted soot particles from a pool jet fire, in cooperation with ONERA. This paragraph summarizes the outputs of this cooperative work (Paulien et al. 2021). In a few words, Table 3 gathers the main laboratory findings, with a lidar *PDR* in the range of 10%. The soot morphology and non-sphericity is clearly seen in Fig. 3 from Paulien et al. (2021) where the minima, which are related to $1-F_{22}^{\lambda}/F_{11}^{\lambda}$, are not null. The retrieved value of the lidar *PDR* interestingly compare with lidar field measurements of the lidar *PDR* by Burton et al. (2016) who retrieved a value of the lidar *PDR* 9.3%

Table 3 First laboratory measurement of the ratio $F_{22}^{\lambda}/F_{11}^{\lambda}$ of scattering matrix elements and corresponding lidar *PDR* of freshly-emitted soots (JET A1 pool fire) at exact backscattering angle $(\theta = \pi)$

Wavelength (nm)	$F_{22}^{\lambda}/F_{11}^{\lambda}$	*PDR*
355	0.79 ± 0.03	11.7 ± 2.3
532	0.84 ± 0.03	8.7 ± 2.1

lidar at 532 nm compatible with our laboratory findings, despite aged smoke was there considered. T-matrix numerical simulations of these aged soot by Mishchenko et al. (2018) also well compare at least at 532 nm. To address the lidar *PDR* of freshly emitted soot, Paulien et al. (2021) applied the superposition T-Matrix (STM) method to numerically simulate the soot aggregates backscattering properties for different soot particles refractive indices, monomer radii and monomer numbers. The range of these parameters which ensures the lowest discrepancy between the laboratory-measured soot lidar *PDR* and the STM-computations was discussed within experimental and numerical error bars. The polydisperse monomers model was found to give an overall better evaluation of the ratio$F_{22}^{\lambda}/F_{11}^{\lambda}$. In the polydisperse case, our numerical and laboratory experimental findings agree at both wavelengths for a refractive index m = 2.65 + i1.32 and monomer number >40 at a mean monomer radius of 30 nm.

3.6 Light Backscattering by Mineral Dust in Laboratory

We here present laboratory experiments on mineral dust at exact backscattering lidar angle using the π-laboratory polarimeter. The motivations of this work are numerous. First of all, revealing the intrinsic lidar *PDR* of mineral dust is necessary for accurate interpretation of lidar returns and for that focusing on the exact lidar backscattering angle in laboratory is essential, as explained in the previous sections. Secondly, for aerosol identification purposes, the dependence of the dust lidar *PDR* has to be analyzed for different dust samples, deferring in sizes and complex refractive index, and for that laboratory intensive work is required (Miffre et al. 2022). Ideally, this laboratory study must be carried out at several lidar wavelengths (355, 532 nm) to better constrain future lidar inversions (Burton et al. 2016). In turn, the ability of the mathematical spheroidal model to reproduce mineral dust particles backscattering at several wavelengths in the exact backward scattering direction may then be discussed. We start from this numerical approach (Miffre et al. 2016).

(a) Ability of the spheroidal model to reproduce the spectral dependence of the dust lidar PDR

In Miffre et al. (2016), using the laboratory π-polarimeter, the lidar *PDR* of two determined particle size distributions of Arizona Test Dust (ATD) were evaluated in laboratory at 355 and 532 nm wavelength simultaneously. Interestingly, these laboratory findings agree with T-matrix numerical simulations, at least for a determined particle size distribution and at a determined wavelength, showing the ability of the spheroidal model to reproduce mineral dust particles in the exact backward scattering direction. However, the spectral dependence of the laboratory-measured *PDR* could not be reproduced with the spheroidal model, even for not evenly distributed aspect ratios.

In more details, we considered a power-law shape distribution of spheroids, i.e.$f(\varepsilon) = \varepsilon^n$, where n is an integer and studied three successive cases: $n = 0$

(equiprobable shape distribution), $n = 3$ then $n = 10$, the latter favoring extreme aspect ratios at the expense of nearly spherical spheroids. After size integration over the particles size distribution (*SD*), the spheroidal model was found capable of reproducing our laboratory experimental results in the exact backscattering direction whatever the radiation wavelength (i.e. either 355 or 532 nm wavelength). The assumption of spheroids evenly distributed over aspect ratio (equiprobable shape distribution) seemed however to decrease the ability of the spheroidal model to account for the particles depolarization. Nevertheless, even by taking into account the spectral dependence of the complex refractive index, the spectral dependence of the dust lidar *PDR* could not be reproduced at both UV and VIS-wavelengths simultaneously. This finding agrees with (Dubovik et al. 2006b), who noted that "the measured spectral dependence (could) only be reproduced by spheroids only if we assume differences for the size distributions for each of the two wavelengths", and was also pointed out in Zubko et al. (2013). Our contribution shows that this statement also applies in the exact backward direction, at least for the particles size distribution considered in this study. As a conclusion, in the exact backward scattering direction, the spheroidal model is well-adapted for reproducing the dust lidar*PDR*, but only at one determined wavelength, either 355 or 532 nm. Readers interested by this specific question can refer to Miffre et al. (2016) for detailed information. We here focus on the dependence of the lidar *PDR* with size and complex refractive index, as presented at the ELS Conference 2021 and in Miffre et al. (2022).

(b) Mineral dust laboratory samples differing in size and mineralogy

To study the dependence of the dust lidar *PDR* with size and mineralogy, we here consider the following mineral dust samples:

- Silica, or silicon oxide (SiO_2), as it is the main pure chemical component present in mineral dust.
- Iron oxide, or hematite (Fe_2O_3), as a secondary pure chemical component present in mineral dust, also selected as a light absorbent in the shortwave spectral region (Zong et al. 2021), which recently gained in interest with papers specifically dedicated to this constituent (Gautam et al. 2020; Go et al. 2022).
- Arizona dust, as it is an important case study of natural mineral dust sample involving a mixture of the above two oxides. Arizona dust is composed of silica (68–76%), while hematite is only weakly present in Arizona dust (2–5%). In short, Arizona dust is hence rather silica-rich.
- Asian dust, as an important case study of natural mineral dust sample, presenting however a lower proportion of silica (34–40%) and a higher proportion of hematite (17–23%). Hence, compared with Arizona dust, Asian dust is more hematite-rich.

To address the dependence of the dust lidar *PDR* with the dust particles size distribution (*SD*), the light backscattered by each above dust sample was measured with the laboratory π-polarimeter in the presence, then in the absence of a cyclone. The retrieved particles *SD* are displayed in Miffre et al. (2022) and are in agreement with the specifications provided by the manufacturers. In the presence of the cyclone, the *SD* is more representative of mineral dust samples after long-range transport, i.e.

Table 4 Laboratory measurement of the ratio $F^{\lambda}_{22}/F^{\lambda}_{11}$ of scattering matrix elements and corresponding lidar PDR(see Eq. 5) for Arizona and Asian dust at exact backscattering angle ($\theta = \pi$), evaluated from the laboratory π-polarimeter (Miffre et al. 2016, 2022)

Mineralogy	λ(nm)	Finer *SD*		Coarser *SD*	
		$F^{\lambda}_{22}/F^{\lambda}_{11}$	*PDR*(%)	$F^{\lambda}_{22}/F^{\lambda}_{11}$	*PDR*(%)
Arizona dust	355	0.514 ± 0.007	32.1 ± 0.6	0.489 ± 0.012	34.3 ± 1.0
	532	0.512 ± 0.012	32.3 ± 1.0	0.464 ± 0.012	36.6 ± 1.1
Asian dust	355	0.603 ± 0.009	24.7 ± 0.6	0.603 ± 0.011	24.8 ± 0.8
	532	0.622 ± 0.009	23.3 ± 0.7	0.558 ± 0.011	28.4 ± 0.8

farther from the dust source regions and will be hereafter referred to as the finer *SD*. Likewise, in the absence of the cyclone, the *SD* corresponds to dust particles closer to dust source regions, will be referred to as the coarser *SD*. The backscattered light intensity was then measured for each dust sample (silica, hematite, Arizona dust, Asian dust) at 355 and 532 nm wavelength for both the finer and the coarser *SD* and the corresponding dust lidar *PDR* was accurately evaluated.

(iii) Laboratory measurement of the lidar PDR of dust particles mixtures at lidar exact backscattering angle

Let us first argue on the retrieved dust lidar *PDR* for Arizona and Asian dust with the coarser *SD*. The variations of the normalized backscattered light intensity by Arizona dust, then Asian dust for the *FinerSD* (left panels) and the *CoarserSD* (right panels) are displayed in Miffre et al. (2022). As above explained, for each light backscattering curve exhibits constant extrema, in each panel, the size and the shape of the dust sample did not vary during the acquisition. As a result, the observed variations relate to the spectral and polarimetric light backscattering characteristics of the considered dust sample and the corresponding experimental data points can be adjusted with Eq. (9) to evaluate $F^{\lambda}_{22,d}/F^{\lambda}_{11,d}$ then the dust lidar *PDR by* applying Eq. (11). Table 4 gathers the retrieved dust lidar *PDR* for Arizona and Asian dust, for the finer and the coarser *SD* at 355 and 532 nm wavelength. The precision on the $F^{\lambda}_{22,d}/F^{\lambda}_{11,d}$ evaluation is remarkable and results from the accuracy of the laboratory π-polarimeter. Care should be taken when comparing the light backscattering curves from Arizona and Asian dust for the applied voltage to the UV and VIS-photodetectors were adjusted to increase the signal-to-noise ratio, as explained in Sect. 3.2. Hence, for the coarser*SD*, the dust lidar *PDR* is higher for Arizona dust. Within experimental error bars, the Arizona and Asian dust lidar *PDR* clearly differ, whatever the chosen wavelength. The generally admitted value of around 33% for the dust lidar *PDR* (Tesche et al. 2009) is indeed observed but for Arizona dust only: Asian dust exhibits a lower depolarization ratio in the range from 24 to 28% depending on the considered *SD* and wavelength. This suggests that the dust lidar *PDR* is primarily governed by the dust particles refractive index. The sensitivity of the dust lidar *PDR* with the considered *SD* is indeed less pronounced: from the coarser to the finer *SD*, a reduction in the dust lidar *PDR* of at most 5% is observed at 532 nm wavelength. At 355 nm wavelength however, the Arizona and Asian dust lidar *PDR* seems practically insensitive to variations in the considered *SD*.

(iv) Laboratory measurement of the lidar PDR of silica and hematite (pure components) at backscattering angle

By applying the same methodology, we retrieved the silica and hematite lidar *PDR* gathered in Table 5 which is the analogue of Table 4 for silica and hematite dust samples. As for Arizona and Asian dust samples, the dust lidar *PDR* for silica and hematite primarily depends on the particles mineralogy and complex refractive index at least at 355 nm wavelength where the silica lidar *PDR* ranges from 23 to 33% depending on the considered *SD* while the hematite lidar *PDR* reaches 10% only. The silica and hematite lidar *PDR* hence strongly depend on the chosen lidar wavelength, with higher depolarization at 355 nm for silica (at 532 nm for hematite). The silica lidar *PDR* strongly depends on the *SD* from the coarser to the finer SD, the reduction in the silica dust lidar PDR reaches 10% at both wavelengths. The dependence of the hematite dust lidar *PDR* with the *SD* is less pronounced, especially at 355 nm wavelength.

(e) Dependence of the dust lidar PDR with size and complex refractive index at exact backscattering angle

The laboratory π-polarimeter however allows discussing on the dependence of the dust lidar *PDR* with the *SD* and complex refractive index (Miffre et al. 2022). Comparing our laboratory findings with other laboratory experiments is not feasible at present to our knowledge, for none of these set-ups operates at lidar exact backscattering angle for aerosols, while the dust lidar *PDR* can be very different at near and exact backscattering angles, as explained in Sect. 1.3. In the literature dedicated to lidar field experiments (Tesche et al. 2009), a dust lidar *PDR* of 33% is often considered in lidar retrievals. This value is indeed measured with our laboratory π-polarimeter for silica oxide, which is the main oxide present in mineral dust, and also for Arizona dust, which is rather silica-rich. Comparison of our laboratory findings with this literature however remains difficult because in lidar field experiments, the measured depolarization is nevertheless that of particle mixtures. Our laboratory findings can however be compared with light scattering numerical simulations,

Table 5 Laboratory measurement of the ratio $F_{22}^{\lambda}/F_{11}^{\lambda}$ of scattering matrix elements and corresponding lidar PDR (see Eq. 5) of silica and hematite at exact backscattering angle ($\theta = \pi$), evaluated from the laboratory π-polarimeter (Miffre et al. 2016, 2022)

Mineralogy	λ (nm)	Finer *SD*		Coarser *SD*	
		$F_{22}^{\lambda}/F_{11}^{\lambda}$	*PDR*(%)	$F_{22}^{\lambda}/F_{11}^{\lambda}$	*PDR*(%)
Silica	355	0.622 ± 0.014	23.3 ± 0.9	0.506 ± 0.011	32.8 ± 1.0
	532	0.751 ± 0.016	14.2 ± 0.9	0.618 ± 0.016	23.6 ± 1.1
Hematite	355	0.805 ± 0.050	10.8 ± 2.5	0.823 ± 0.015	9.7 ± 0.7
	532	0.652 ± 0.055	21.1 ± 3.5	0.715 ± 0.019	16.6 ± 1.1

which are becoming more and more accurate. Light scattering numerical simulations (Kahnert 2015) show that the dust lidar *PDR* is strongly modulated by the particles inhomogeneity, especially in the presence of hematite. In Kahnert (2015), it was stressed that this feature was particularly pronounced in the lidar backward scattering direction and our laboratory findings show that the dust lidar *PDR* is indeed strongly modulated by the particles inhomogeneity. In the most general case, the dust lidar *PDR* appears as a complex function of the particles mineralogy, size distribution and wavelength Though this triple dependence is difficult to disentangle, based on our laboratory findings, we see that the mineralogy primarily affects the dust lidar, at least when hematite is involved. Indeed, hematite is a light absorbent and the presence of an imaginary part for the complex refractive index of hematite modifies the backscattering matrix elements, so does the corresponding dust lidar*PDR*. In turn, Asian dust, which is more hematite rich than Arizona dust, exhibits a lower depolarization ratio. The impact of hematite on dust absorption wavelengths ranging from 0.2 to 1.0 µm was indeed recently evaluated in the literature using the T-matrix spheroidal model by Zong et al. (2021). Hence and as a result, when hematite, which is a light absorbent, is present, it mainly governs the depolarization ratio, though size and wavelength effects also clearly play a role.

4 Light Backscattering in the Atmosphere: Lidar Field Experiments

4.1 Atmospheric Lidar Implications

(a) Circular versus linear depolarization ratio

The above laboratory measurements at near ($\theta < \pi$) and exact backscattering ($\theta = \pi$) allow retrieved the linear and circular particles depolarization ratios which are used in lidar applications. Following Mishchenko and Hovenier [36], the linear *PDR*(here noted $\delta_L(\pi)$ for lidar purposes) and circular $\delta_C(\pi)$ ddepolarization ratios relate to the laboratory measurements at scattering angle θ as follows:

$$\begin{aligned} \delta_L(\theta) &= (1 - f_{22}^{\lambda}(\theta)/\big(1 \pm 2f_{12}^{\lambda}(\theta) + f_{22}^{\lambda}(\theta)\big) \\ \delta_C(\theta) &= \big(1 \pm f_{44}^{\lambda}(\theta)\big)/\big(1 \mp f_{44}^{\lambda}(\theta)\big) \end{aligned} \tag{14}$$

where reduced notations have been used ($f_{ij}^{\lambda} = F_{ij}^{\lambda}/F_{11}^{\lambda}$) and the positive (negative) sign corresponds to incident p (s) polarization state for *PDR* and to incident RC (LC) polarization state for PDR_C. From Fig. 7 from Miffre et al. (2019b), at exact backscattering ($\theta = \pi$),$\delta_L(\pi) = (27.3 \pm 1.6)\%$ while $\delta_C(\pi) = (75.4 \pm 6.1)\%$. The circular depolarization ratio δ_c exhibits pronounced variations, due to variations in $f_{44}(\theta)$, increasing from 62.6% at 176.0° scattering angle up to 75.4% at 180.0°. For the first time to our knowledge, within our experimental error bars, we may conclude that the relationship $\delta_C(\pi) = 2\delta_L(\pi)/(1 - \delta_L(\pi))$ only applies at exact backscattering angle, as theoretically set by Mishchenko and Hovenier (1995). In what follows, the lidar linear *PDR* will be noted δ for $\delta_L(\pi)$.

(b) Lidar partitioning algorithms

The downside of such field lidar depolarization measurements is that the measured depolarization ratio is nevertheless that of a mixture. Hence, care should be taken when comparing the lidar-measured depolarization ratio with our laboratory findings, which reveal the intrinsic depolarization ratio of a determined size and shape distribution of a given aerosol, as we demonstrated (Mehri et al. 2018; Miffre et al. 2011). The intrinsic depolarization ratio remains key for precise retrievals of vertical profiles of atmospheric particles backscattering dedicated to a given aerosol, for instance mineral dust (David et al. 2013; Mehri et al. 2018; Miffre et al. 2011).

Hence, lidar partitioning algorithms have been developed to disentangle particle mixtures. Our group contributed to that research field in line of (Tesche et al. 2009) 's contribution by developing the $1\beta + 1\delta$ partitioning algorithm. Moreover, we extended this approach to three-component particle external mixtures by developing the 2 $\beta + 2\delta$ partitioning algorithm (David et al. 2013). We here briefly present the 1 $\beta + 1\delta$ partitioning algorithm. Interested readers can find more details in the corresponding publications (Mehri et al. 2018; Miffre et al. 2011).

Let us consider a two-component particle external mixture$(p) = \{s, ns\}$, composed of both spherical (s) and nonspherical (ns)-particles of different origin. After long-range transport, an example such a mixture is given by the external mixing of mineral dust (d) particles with spherical (s) particles, most likely hydrated sulfates. To quantify the contribution of mineral dust particles in the two-component particle external mixture$(p) = \{s, ns\}$, a careful analysis of the polarization of the backscattered radiation must be performed. The starting point is the lidar observable, the lidar particles backscattering coefficient:

$$\beta_p = \int_{SD} \mathrm{C}_{back,p} n_p(r)dr \cdot = \int_{SD} \mathrm{C}_{sca,p} \frac{F_{11,p}}{4\pi} n_p(r)dr \tag{15}$$

where $C_{back,p}$ is the particle backscattering cross-section and the dependence with wavelength λ has been omitted to ease the reading. A polarization lidar experiment at wavelength λ provides accurate vertical profiles of polarization-resolved particles backscattering $\beta_{p,//}$ and $\beta_{p,\perp}$, on each $\pi = (//, \perp)$ polarization channel, defined with respect to the laser linear polarization. Noting that β_p is additive and that $\delta_{ns} = \beta_{ns,\perp}/\beta_{ns,//}$, we get (David et al. 2013; Miffre et al. 2011):

$$\beta_{ns} = \beta_{p,\perp}(1 + 1/\delta_{ns}) \tag{16}$$

As a result, vertical profiles of particles backscattering specific to non-spherical mineral dust can be retrieved by coupling polarization-resolved particles backscattering $\beta_{p,\perp}$ with accurate laboratory measurements of the intrinsic dust lidar *PDR*, as presented in Sect. 3. Examples of applications of this approach are here detailed, using the Lyon (France) lidar station, the only to our knowledge whose polarization lidar detector is based on the laboratory π-polarimeter.

4.2 Field Version of the Laboratory π-polarimeter

As show in David et al. (2012; Miffre et al. 2019a), a field version of the laboratory π-polarimeter presented in Sect. 3 has been implemented as lidar detector, to avoid any possible bias when exploiting the synergy between laboratory and field experiments. This approach allowed to specify the polarization and wavelengths cross-talks of our lidar detector in laboratory, in the form of a detector transfer matrix, relating the entrance I_π^λ and output $\left(I_\pi^\lambda\right)^*$ intensity of the π-polarimeter (David et al. 2012):

$$\begin{bmatrix} \left(I_p^{355nm}\right)^* \\ \left(I_s^{355nm}\right)^* \\ \left(I_p^{532nm}\right)^* \\ \left(I_s^{532nm}\right)^* \end{bmatrix} = \begin{bmatrix} \eta_p(355nm) & 0 & 0 & 0 \\ 4\times10^{-8} & \eta_s(355nm) & 0 & 0 \\ 0 & 0 & \eta_p(532nm) & 0 \\ 0 & 0 & 0 & \eta_s(532nm) \end{bmatrix} \begin{bmatrix} I_p^{355nm} \\ I_s^{355nm} \\ I_p^{532nm} \\ I_s^{532nm} \end{bmatrix} \tag{17}$$

The detector transfer matrix being diagonal (with 4×10^{-8} accuracy), wavelength and polarization cross-talks are negligible, which allows a robust calibration of the lidar *PDR* to be achieved, as published in (Miffre et al. 2019a). This calibration consists in evaluating the electro-optics gain calibration constant G of the lidar detector at wavelength λ to retrieve the intrinsic lidar *PDR* from the measured lidar δ^*. In the literature, existing calibration methods rely on a molecular atmosphere (Behrendt and Nakamura 2002), which however does not rigorously exist, or on the ±45° methodology (Freudenthaler et al. 2009), which may saturate the photodetector. Rather, we proposed and successfully applied the methodology illustrated in Fig. 1 in Miffre et al. (2019a). At wavelength λ, a precise evaluation of G is achieved by introducing controlled amounts of polarization cross-talks, using a half-wavelength plate (HWP), inserted on the optical pathway from the laser to the atmosphere. The variations of the measured atmospheric depolarization δ^* with the modulation angle φ of the HWP can then be adjusted in the framework of the scattering matrix formalism to get precise value of G. Indeed, the lidar intensity detected at wavelength λ on each $\pi = (p, s)$polarization channel is given by:

$$I_\pi = \frac{\eta_\pi P_{0,\lambda}}{z}\left(P_j\right)[PBC][F_\lambda(\theta = \pi)][HWP][St_i] \tag{18}$$

where, as in Sects. 2 and 3, $[\boldsymbol{PBC}]$ and $[\boldsymbol{HWP}]$ are the Mueller matrices of the polarizing beam-splitter cube (PBC) and the HWP respectively while $(St_i) = [1, 1, 0, 0]^T$.

In Eq. (19), η_π is the optoelectronics constant of the π-polarization channel (defined with respect to the incident laser polarization) and the gain-optics calibration constant G relates to this quantity as $\mathrm{G} = \eta_s/\eta_p$. The measured depolarization is then $\delta^* = I_s/I_p$ is then retrieved by using Eq. (5) to replace $F_{22}^{\lambda}/F_{11}^{\lambda}$ as a function of the lidar *PDR*. Hence, at wavelength λ, the measured atmospheric depolarization δ^* relates to the intrinsic particles depolarization δ as follows:

$$\delta^* = G\frac{1 + \delta - (1 - \delta)\cos(4\varphi)}{1 + \delta + (1 - \delta)\cos(4\varphi)} \tag{19}$$

As a result, the calibration constant G can be evaluated at wavelength λ with 2% accuracy by adjusting the φ-variations of the measured δ^* with Eq. (20), as illustrated in Fig. 1 from Miffre et al. (2019a) at 355 and 532 nm wavelength. The sensitivity of our laboratory π-polarimeter, when combined with this accurate calibration, allowed to reveal accurate vertical profiles of particles depolarization ratios directly in the atmosphere from volcanic ashes released from the Icelandic volcano (Miffre et al. 2012), mineral dust particles brought to France from Saharan dust outbreaks (David et al. 2013; Mehri et al. 2018), or even the subsequent growth following new particle formation events promoted by mineral dust (Miffre et al. 2019a).

4.3 Application Case Study: Time-Altitude Maps of Dust Particles Backscattering Revealing the Underlying Complex Physical-Chemistry

We here evaluate the dust particles backscattering coefficient corresponding to a Saharan dust outbreak that occurred at Lyon in July 2010. During this event, non-spherical particles were identified as desert dust particles, as confirmed by air mass back-trajectories as published in Dupart et al. (2012) as a supplementary material. Figure 4 from David et al. (2014) presents the corresponding time-altitude maps of the lidar-retrieved backscattering coefficients, measured at Lyon at λ = 355 nm in July 2010 during a Saharan dust outbreak by taking benefit from the laboratory π-polarimeter. Mineral dust particles, for which $\beta_{\mathrm{p},.}$ is not null, are mainly located above 3 km altitude while a $\beta_{\mathrm{p},//}$-enhancement is observable in the free troposphere between 2 and 3 km altitude, which is not observed on the $\beta_{\mathrm{p},\perp}$-map. Interestingly, an enhancement is to be seen in the time-altitude map corresponding to non-dust particles, which are spherical. We could relate this behavior to the subsequent growth following a new particle formation event promoted by mineral dust through a photo-catalytic process (Dupart et al. 2012). Interested readers can find more information in the corresponding publications (David et al. 2014; Miffre et al. 2019a, 2020). As a conclusion, the laboratory approach we followed with the laboratory π-polarimeter enables to reveal the underlying physico-chemical processes involved in the atmosphere, which in turn reinforces our understanding of light backscattering by such complex-shaped particles.

5 Conclusion and Outlooks

This book chapter is dedicated to light backscattering by atmospheric particles. This research topic is extremely important for both fundamental and applicative purposes:

- From a fundamental point of view, light backscattering has proven efficiency for providing information on the optical properties of condensed or gaseous matter (Vitkin and Studinski 2001; Wang et al. 2012) and also as involved in the so-called coherent backscattering effect [8], which is still to be understood. Also, near and exact backscattering are interesting to study as light scattering numerical simulations exhibit a narrow double-lobe feature when studying small-scale surface roughness [16]. Finally, for radiative transfer purposes, the scattering phase function needs to be precisely known over the whole scattering angle range, and hence covers the backward scattering direction with precision.
- From an applicative point of view, light backscattering is the key physical process involved in ground-based and satellite-based lidar remote sensing instruments which provide a major source of global data on mineral dust, which are needed for radiative and climate forcing assessments.

While a large number of references exist in the literature on light scattering numerical simulations and on lidar remote sensing data at backscattering angle, there is a dearth of laboratory experiments providing the so-called lidar *PDR* at exact lidar backscattering angle ($\theta = \pi$). On account of the above considerations, after reviewing the corresponding literature, this book chapter mainly focuses on controlled laboratory experiments at near ($\theta < \pi$) and exact ($\theta = \pi$) backscattering angles for particles embedded in ambient air.

- In Sect. 2, to complement existing laboratory light scattering experimental set-ups, we then proposed a new laboratory experiment, the π+ε-laboratory polarimeter (Miffre et al. 2019a, b), to retrieve the scattering matrix elements $F^{\lambda}_{ij}/F^{\lambda}_{11}(\theta)$ from 176.0° to backscattering angle with a 0.4° angular step for mineral dust. The ability of the mathematical spheroidal model to mimic light scattering by mineral dust at near backscattering angles is then verified.
- In Sect. 3, we specifically focused on the cutting-edge laboratory π-polarimeter at exact backscattering angle or lidar angle ($\theta = \pi$), (Miffre et al. 2016), with emphasis on its ability to accurately measure the backscattered light intensity and the corresponding lidar *PDR* of aerosols. Case studies on spherical inorganic sulfates, core–shell organic sulfates (Dubois et al. 2021), freshly-emitted soot (Paulien et al. 2021) and mineral dust (Miffre et al. 2022) were studied. In the latter study, the dependence of the lidar PDR with size and complex refractive index was

studied in laboratory for the first time to our knowledge at exact backscattering lidar angle ($\theta = \pi$).

- In Sect. 4, implications of this laboratory work on aerosols light backscattering in lidar remote sensing experiments were proposed and discussed. There, the sensitivity and accuracy achieved on the laboratory π-polarimeter at exact backscattering angle allowed providing calibrated polarization lidar measurements, which in turn have the ability to reveal the underlying complex vertical layering of the atmosphere (David et al. 2014; Miffre et al. 2019a, 2020). In particular, while the vertical layering of the atmosphere is extremely complex, vertical profiles specific to non-spherical particles backscattering could be accurately retrieved by taking benefit from the laboratory π-polarimeter.

We hope that this work will contribute to provide a better understanding of the physical process of light backscattering and may provide accurate inputs to better constrain lidar inversions. Still, lots of work need to be done in laboratory to better understand the dependence of the lidar *PDR* with the particles size and complex refractive index at specific backscattering angle, a direction particularly sensitive to particles inhomogeneity. In this context, a first interesting complementary step would be to extend the applicability of the laboratory π-polarimeter to the 1064 nm wavelength, to better constraint both light scattering numerical simulations and lidar inversions.

References

Ackerman TP, Toon OB (1981) Absorption of visible radiation in atmosphere containing mixtures of absorbing and nonabsorbing particles. Appl Opt 20:3661. https://doi.org/10.1364/AO.20.003661

Ansmann A, Petzold A, Kandler K, Tegen I, Wendisch M, Müller D, Weinzierl B, Müller T, Heintzenberg J (2011) Saharan Mineral Dust Experiments SAMUM–1 and SAMUM–2: what have we learned? Tellus B Chem. Phys Meteorol 63:403–429. https://doi.org/10.1111/j.1600-0889.2011.00555.x

Behrendt A, Nakamura T (2002) Calculation of the calibration constant of polarization lidar and its dependency on atmospheric temperature. Opt Express 10:805–817. https://doi.org/10.1364/OE.10.000805

Bohren CF, Huffman DR (1983) Absorption and scattering of light by small particles. Wiley-VCH, Weinheim

Burton SP, Chemyakin E, Liu X, Knobelspiesse K, Stamnes S, Sawamura P, Moore RH, Hostetler CA, Ferrare RA (2016) Information content and sensitivity of the 3 $\beta + 2\ \alpha$ lidar measurement system for aerosol microphysical retrievals. Atmos Meas Tech 9:5555–5574. https://doi.org/10.5194/amt-9-5555-2016

Chien C-H, Theodore A, Wu C-Y, Hsu Y-M, Birky B (2016) Upon correlating diameters measured by optical particle counters and aerodynamic particle sizers. J Aerosol Sci 101:77–85. https://doi.org/10.1016/j.jaerosci.2016.05.011

Cholleton D, Bialic E, Dumas A, Kaluzny P, Rairoux P, Miffre A (2020) Laboratory evaluation of the (VIS, IR) scattering matrix of complex-shaped ragweed pollen particles. J Quant Spectrosc Radiat Transf 254:107223. https://doi.org/10.1016/j.jqsrt.2020.107223

Cholleton D, Bialic É, Dumas A, Kaluzny P, Rairoux P, Miffre A (2022) Laboratory evaluation of the scattering matrix of ragweed, ash, birch and pine pollen towards pollen classification. Atmos Meas Tech 15:1021–1032. https://doi.org/10.5194/amt-15-1021-2022

Cotterell MI, Willoughby RE, Bzdek BR, Orr-Ewing AJ, Reid JP (2017) A complete parameterisation of the relative humidity and wavelength dependence of the refractive index of hygroscopic inorganic aerosol particles. Atmos Chem Phys 17:9837–9851. https://doi.org/10.5194/acp-17-9837-2017

Dabrowska DD, Muñoz O, Moreno F, Nousiainen T, Zubko E, Marra AC (2013) Experimental and simulated scattering matrices of small calcite particles at 647nm. J Quant Spectrosc Radiat Transf 124:62–78. https://doi.org/10.1016/j.jqsrt.2013.02.010

David G (2013) Polarization-resolved backscattering from nanoparticles in the atmosphere: field and laboratory experiments

David G, Miffre A, Thomas B, Rairoux P (2012) Sensitive and accurate dual-wavelength UV-VIS polarization detector for optical remote sensing of tropospheric aerosols. Appl Phys B 108:197–216. https://doi.org/10.1007/s00340-012-5066-x

David G, Thomas B, Dupart Y, D'Anna B, George C, Miffre A, Rairoux P (2014) UV polarization lidar for remote sensing new particles formation in the atmosphere. Opt Express 22:A1009. https://doi.org/10.1364/OE.22.0A1009

David G, Thomas B, Nousiainen T, Miffre A, Rairoux P (2013) Retrieving simulated volcanic, desert dust and sea-salt particle properties from two/three-component particle mixtures using UV-VIS polarization lidar and T matrix. Atmos Chem Phys 13:6757–6776. https://doi.org/10.5194/acp-13-6757-2013

Dubois C, Cholleton D, Gemayel R, Chen Y, Surratt JD, George C, Rairoux P, Miffre A, Riva M (2021) Decrease in sulfate aerosol light backscattering by reactive uptake of isoprene epoxydiols. Phys Chem Chem Phys 23:5927–5935. https://doi.org/10.1039/D0CP05468B

Dubovik O, Sinyuk A, Lapyonok T, Holben BN, Mishchenko M, Yang P, Eck TF, Volten H, Muñoz O, Veihelmann B, van der Zande WJ, Leon J-F, Sorokin M, Slutsker I (2006a) Application of spheroid models to account for aerosol particle nonsphericity in remote sensing of desert dust. J Geophys Res 111:D11208. https://doi.org/10.1029/2005JD006619

Dubovik O, Sinyuk A, Lapyonok T, Holben BN, Mishchenko M, Yang P, Eck TF, Volten H, Muñoz O, Veihelmann B, van der Zande WJ, Leon J-F, Sorokin M, Slutsker I (2006b) Application of spheroid models to account for aerosol particle nonsphericity in remote sensing of desert dust. J Geophys Res Atmos 111. https://doi.org/10.1029/2005JD006619

Dupart Y, King SM, Nekat B, Nowak A, Wiedensohler A, Herrmann H, David G, Thomas B, Miffre A, Rairoux P, D'Anna B, George C (2012) Mineral dust photochemistry induces nucleation events in the presence of SO2. Proc Natl Acad Sci U S A 109:20842–20847. https://doi.org/10.1073/pnas.1212297109

Freudenthaler V, Esselborn M, Wiegner M, Heese B, Tesche M, Ansmann A, MüLLER D, Althausen D, Wirth M, Fix A, Ehret G, Knippertz P, Toledano C, Gasteiger J, Garhammer M, Seefeldner M (2009) Depolarization ratio profiling at several wavelengths in pure Saharan dust during SAMUM 2006. Tellus B Chem Phys Meteorol 61:165–179. https://doi.org/10.1111/j.1600-0889.2008.00396.x

Fu R, Wang C, Muñoz O, Videen G, Santarpia JL, Pan YL (2017) Elastic back-scatteringpatterns via particle surface roughness and orientation from single trapped airborne aerosol particles. J Quant Spectro Radiat Transfer 187:224–231

Gasteiger J, Wiegner M, GROß S, Freudenthaler V, Toledano C, Tesche M, Kandler K (2011) Modelling lidar-relevant optical properties of complex mineral dust aerosols. Tellus Ser B Chem Phys Meteorol 63:725–741. https://doi.org/10.1111/j.1600-0889.2011.00559.x

Gautam P, Maughan JB, Ilavsky J, Sorensen CM (2020) Light scattering study of highly absorptive, non-fractal, hematite aggregates. J Quant Spectrosc Radiat Transf 246:106919. https://doi.org/10.1016/j.jqsrt.2020.106919

Glen A, Brooks SD (2013) A new method for measuring optical scattering properties of atmospherically relevant dusts using the Cloud and Aerosol Spectrometer with Polarization (CASPOL). Atmos Chem Phys 13:1345–1356. https://doi.org/10.5194/acp-13-1345-2013

Go S, Lyapustin A, Schuster GL, Choi M, Ginoux P, Chin M, Kalashnikova O, Dubovik O, Kim J, da Silva A, Holben B, Reid JS (2022) Inferring iron-oxide species content in atmospheric mineral dust from DSCOVR EPIC observations. Atmos Chem Phys 22:1395–1423. https://doi.org/10.5194/acp-22-1395-2022

Gómez Martín JC, Guirado D, Frattin E, Bermudez-Edo M, Cariñanos Gonzalez P, Olmo Reyes FJ, Nousiainen T, Gutiérrez PJ, Moreno F, Muñoz O (2021) On the application of scattering matrix measurements to detection and identification of major types of airborne aerosol particles: Volcanic ash, desert dust and pollen. J Quant Spectrosc Radiat Transf 271:107761. https://doi.org/10.1016/j.jqsrt.2021.107761

Haarig M, Ansmann A, Baars H, Jimenez C, Veselovskii I, Engelmann R, Althausen D (2018) Depolarization and lidar ratios at 355, 532, and 1064 nm and microphysical properties of aged tropospheric and stratospheric Canadian wildfire smoke. Atmos Chem Phys 18:11847–11861. https://doi.org/10.5194/acp-18-11847-2018

Haarig M, Ansmann A, Engelmann R, Baars H, Toledano C, Torres B, Althausen D, Radenz M, Wandinger U (2022) First triple-wavelength lidar observations of depolarization and extinction-to-backscatter ratios of Saharan dust. Atmos Chem Phys 22:355–369. https://doi.org/10.5194/acp-22-355-2022

Hofer J, Ansmann A, Althausen D, Engelmann R, Baars H, Fomba, KW, Wandinger U, Abdullaev SF, Makhmudov AN (2020) Optical properties of Central Asian aerosol relevant for spaceborne lidar applications and aerosol typing at 355 and 532 nm. Atmos Chem Phys 20:9265–9280. https://doi.org/10.5194/acp-20-9265-2020

Huang X, Yang P, Kattawar G, Liou K-N (2015) Effect of mineral dust aerosol aspect ratio on polarized reflectance. J Quant Spectrosc Radiat Transf 151:97–109. https://doi.org/10.1016/j.jqsrt.2014.09.014

Huang Y, Liu C, Yao B, Yin Y, Bi L (2020) Scattering matrices of mineral dust aerosols: a refinement of the refractive index impact. Atmos Chem Phys 20:2865–2876. https://doi.org/10.5194/acp-20-2865-2020

Hunt AJ (1973) A new polarization-modulated light scattering instrument. Rev Sci Instrum 44:1753. https://doi.org/10.1063/1.1686049

IPCC (2013) Climate change 2013: the physical science basis: Working Group I contribution to the Fifth Assessment Report of the Intergovernmental Panel on Climate Change. Cambridge Univ. Press, New York, NY.

Järvinen E, Kemppinen O, Nousiainen T, Kociok T, Möhler O, Leisner T, Schnaiter M (2016) Laboratory investigations of mineral dust near-backscattering depolarization ratios. J Quant Spectrosc Radiat Transf Electromagnetic Light Scattering Nonspherical Particles XV: Celebrating 150 years of Maxwell's electromagnetics 178:192–208. https://doi.org/10.1016/j.jqsrt.2016.02.003

Kahnert M (2015) Modelling radiometric properties of inhomogeneous mineral dust particles: Applicability and limitations of effective medium theories. J Quant Spectrosc Radiat Transf 152:16–27. https://doi.org/10.1016/j.jqsrt.2014.10.025

Kahnert M, Kanngießer F, Järvinen E, Schnaiter M (2020) Aerosol-optics model for the backscatter depolarisation ratio of mineral dust particles. J Quant Spectrosc Radiat Transf 254:107177. https://doi.org/10.1016/j.jqsrt.2020.107177

Kahnert M, Nousiainen T, Lindqvist H (2014) Review: Model particles in atmospheric optics. J Quant Spectrosc Radiat Transf 146:41–58. https://doi.org/10.1016/j.jqsrt.2014.02.014

Kahnert M, Nousiainen T, Räisainen P (2007) Mie simulations as an error source in mineral aerosol radiative forcing calculations. QJR 133:299–307. https://doi.org/10.1002/qj.40

Kahnert M, Nousiainen T, Thomas MA, Tyynelä J (2012) Light scattering by particles with small-scale surface roughness: comparison of four classes of model geometries. J Quant Spectrosc Radiat Transf Electromagnetic Light Scatter Non-Spherical Particles XIII 113:2356–2367. https://doi.org/10.1016/j.jqsrt.2012.03.017

Kahnert M, Rother T (2011) Modeling optical properties of particles with small-scale surface roughness: combination of group theory with a perturbation approach. Opt Express 19:11138–11151. https://doi.org/10.1364/OE.19.011138

Kemppinen O, Nousiainen T, Lindqvist H (2015) The impact of surface roughness on scattering by realistically shaped wavelength-scale dust particles. J Quant Spectrosc Radiat Transf 150:55–67. https://doi.org/10.1016/j.jqsrt.2014.05.024

Kuga Y, Ishimaru A (1984) Retroreflectance from a dense distribution of spherical particles. J Opt Soc Am A 1:831–835

Laan EC, Volten H, Stam DM, Muñoz O, Hovenier JW, Roush TL (2009) Scattering matrices and expansion coefficients of martian analogue palagonite particles. Icarus 199:219–230. https://doi.org/10.1016/j.icarus.2008.08.011

Liou K, Lahore H (1974) Laser sensing of cloud composition: a backscattered depolarization technique. J Appl Meteorol

Liu C, Lee Panetta R, Yang P (2014) Inhomogeneity structure and the applicability of effective medium approximations in calculating light scattering by inhomogeneous particles. J Quant Spectrosc Radiat Transf 146:331–348. https://doi.org/10.1016/j.jqsrt.2014.03.018

Liu L, Mishchenko MI, Hovenier JW, Volten H, Muñoz O (2003) Scattering matrix of quartz aerosols: comparison and synthesis of laboratory and Lorenz-Mie results. J Quant Spectrosc Radiat Transf 79–80:911–920. https://doi.org/10.1016/S0022-4073(02)00328-X

Liu L, Mishchenko MI (2018) Scattering and radiative properties of morphologically complex carbonaceous aerosols: a systematic modeling study. Remote Sens 10(10). https://doi.org/10.3390/rs10101634

Mehri T (2018) Rétrodiffusion (UV, VIS) résolue en polarisation de particules d'origine désertique: expériences de laboratoire et en atmosphère réelle par lidar

Mehri T, Kemppinen O, David G, Lindqvist H, Tyynelä J, Nousiainen T, Rairoux P, Miffre A (2018) Investigating the size, shape and surface roughness dependence of polarization lidars with light-scattering computations on real mineral dust particles: Application to dust particles' external mixtures and dust mass concentration retrievals. Atmospheric Res 203:44–61. https://doi.org/10.1016/j.atmosres.2017.11.027

Merikallio S, Lindqvist H, Nousiainen T, Kahnert M (2011) Modelling light scattering by mineral dust using spheroids: assessment of applicability. Atmospheric Chem. Phys. 11:5347–5363. https://doi.org/10.5194/acp-11-5347-2011

Mie G (1908) Beiträge zur Optik trüber Medien, speziell kolloidaler Metallösungen. Ann Phys 330:377–445. https://doi.org/10.1002/andp.19083300302

Miffre A, Cholleton D, Mehri T, Rairoux P (2019a) Remote Sensing Observation of New Particle Formation Events with a (UV, VIS) Polarization Lidar. Remote Sens 11:1761. https://doi.org/10.3390/rs11151761

Miffre A, Cholleton D, Noel, C. and Rairoux P (2022) Investigating the dependence of mineral dust depolarization on complex refractive index and size with a laboratory polarimeter at 180.0° lidar backscattering angle, submitted to Atmos Meas Tech

Miffre A, Cholleton D, Rairoux P (2020) On the use of light polarization to investigate the size, shape, and refractive index dependence of backscattering Ångström exponents. Opt Lett 45:1084. https://doi.org/10.1364/OL.385107

Miffre A, Cholleton D, Rairoux P (2019b) Laboratory evaluation of the scattering matrix elements of mineral dust particles from 176.0° up to 180.0°-exact backscattering angle. J Quant Spectrosc Radiat Transf 222–223:45–59. https://doi.org/10.1016/j.jqsrt.2018.10.019

Miffre A, David G, Thomas B, Rairoux P (2011) Atmospheric non-spherical particles optical properties from UV-polarization lidar and scattering matrix. Geophys Res Lett 38:L16804. https://doi.org/10.1029/2011GL048310

Miffre A, David G, Thomas B, Rairoux P, Fjaeraa AM, Kristiansen NI, Stohl A (2012) Volcanic aerosol optical properties and phase partitioning behavior after long-range advection characterized by UV-Lidar measurements. Atmos Environ 48:76–84. https://doi.org/10.1016/j.atmosenv.2011.03.057

Miffre A, Mehri T, Francis M, Rairoux P (2016) UV–VIS depolarization from Arizona Test Dust particles at exact backscattering angle. J Quant Spectrosc Radiat Transf 169:79–90. https://doi.org/10.1016/j.jqsrt.2015.09.016

Mishchenko MI (2009) Electromagnetic scattering by nonspherical particles: a tutorial review. J Quant Spectrosc Radiat Transf 110:808–832. https://doi.org/10.1016/j.jqsrt.2008.12.005

Mishchenko MI, Hovenier JW (1995) Depolarization of light backscattered by randomly oriented nonspherical particles. Opt Lett 20:1356. https://doi.org/10.1364/OL.20.001356

Mishchenko MI, Hovenier JW, Mackowski DW (2004a) Single scattering by a small volume element. J Opt Soc Am A Opt Image Sci Vis 21:71–87. https://doi.org/10.1364/JOSAA.21.000071

Mishchenko MI, Liu L, Travis LD, Lacis AA (2004b) Scattering and radiative properties of semi-external versus external mixtures of different aerosol types. J Quant Spectrosc Radiat Transf 88:139–147. https://doi.org/10.1016/j.jqsrt.2003.12.032

Mishchenko MI, Liu L, Videen G (2007) Conditions of applicability of the single-scattering approximation. Opt Express 15:7522. https://doi.org/10.1364/OE.15.007522

Mishchenko MI, Travis L, Lacis A (2002) Scattering, absorption, and emission of light by small particles. Cambridge

Mishchenko MI, Travis LD (1998) Capabilities and limitations of a current FORTRAN implementation of the T-matrix method for randomly oriented, rotationally symmetric scatterers. J Quant Spectrosc Radiat Transf 60:309–324. https://doi.org/10.1016/S0022-4073(98)00008-9

Mishchenko MI, Dlugach ZM, Zakharova NT (2013) Direct demonstration of the concept of unrestricted effective-medium approximations. Opt Lett 39:3935–3938

Monge M, Rosenorn T, Favez O, Müller M, Adler G, Abo Riziq A, Rudich Y, Hermann H, George C, D'Anna B (2012) Alternative pathway for atmospheric particles growth. Proc 109, 6840–4. https://doi.org/10.1073/pnas.1120593109

Müller D, Veselovskii I, Kolgotin A, Tesche M, Ansmann A, Dubovik O (2013) Vertical profiles of pure dust and mixed smoke–dust plumes inferred from inversion of multiwavelength Raman/polarization lidar data and comparison to AERONET retrievals and in situ observations. Appl Opt 52:3178. https://doi.org/10.1364/AO.52.003178

Muñoz O, Hovenier JW (2011) Laboratory measurements of single light scattering by ensembles of randomly oriented small irregular particles in air: a review. J Quant Spectrosc Radiat Transf 112:1646–1657. https://doi.org/10.1016/j.jqsrt.2011.02.005

Nakayama T, Sato K, Imamura T, Matsumi Y (2018) Effect of oxidation process on complex refractive index of secondary organic aerosol generated from isoprene. Environ Sci Technol 52:2566–2574. https://doi.org/10.1021/acs.est.7b05852

Nousiainen T (2009) Optical modeling of mineral dust particles: a review. J Quant Spectrosc Radiat Transf 110:1261–1279. https://doi.org/10.1016/j.jqsrt.2009.03.002

Olson N, Lei Z, Craig RL, Zhang Y, Chen Y, Lambe AT, Zhang Z, Gold A, Surratt JD, Ault AP (2019) Reactive uptake of isoprene epoxydiols increases the viscosity of the core of phase-separated aerosol particles. ACS Earth Space Chem. acsearthspacechem.9b00138. https://doi.org/10.1021/acsearthspacechem.9b00138

Ovadnevaite J, Ceburnis D, Plauskaite-Sukiene K, Modini R, Dupuy R, Rimselyte I, Ramonet M, Kvietkus K, Ristovski Z, Berresheim H, O'Dowd CD (2009) Volcanic sulphate and arctic dust plumes over the North Atlantic Ocean. Atmos Environ 43:4968–4974. https://doi.org/10.1016/j.atmosenv.2009.07.007

Paulien L, Ceolato R, Fossard F, Rairoux P, Miffre A (2021) (UV, VIS) Laboratory evaluation of the lidar depolarization ratio of freshly emitted soot aggregates from pool fire in ambient air at exact backscattering angle. J Quant Spectrosc Radiat Transf 260:107451. https://doi.org/10.1016/j.jqsrt.2020.107451

Perry R, Hunt A, Huffman D (1978) Experimental determinations of Mueller scattering matrices for nonspherical particles. Appl Opt 17:2700–2710. https://doi.org/10.1364/AO.17.002700

Räisänen P, Haapanala P, Chung CE, Kahnert M, Makkonen R, Tonttila J, Nousiainen T (2013) Impact of dust particle non-sphericity on climate simulations. QJR Meteorol Soc 139:2222–2232. https://doi.org/10.1002/qj.2084

Riva M, Chen Y, Zhang Y, Lei Z, Olson N, Boyer HC, Narayan S, Yee LD, Green H, Cui T, Zhang Z, Baumann KD, Fort M, Edgerton ES, Budisulistiorini S, Rose CA, Ribeiro I, de Oliveira RL, Santos E, Szopa S, Machado C, Zhao Y, Alves E, de Sa S, Hu W, Knipping E, Shaw S, Duvoisin Junior S, Souza RAF. de Palm BB, Jimenez JL, Glasius M, Goldstein AH, Pye HOT, Gold A, Turpin BJ, Vizuete W, Martin ST, Thornton J, Dutcher CS, Ault AP, Surratt JD (2019) Increasing Isoprene Epoxydiol-to-Inorganic Sulfate Aerosol (IEPOX:Sulf $_{\text{inorg}}$) ratio results in extensive conversion of inorganic sulfate to organosulfur forms: implications for aerosol physicochemical properties. Environ Sci Technol acs.est.9b01019. https://doi.org/10.1021/acs.est.9b01019

Saito M, Yang P, Ding J, Liu X (2021) A comprehensive database of the optical properties of irregular aerosol particles for radiative transfer simulations. J Atmos Sci 78:2089–2111. https://doi.org/10.1175/JAS-D-20-0338.1

Sakai T, Nagai T, Zaizen Y, Mano Y (2010) Backscattering linear depolarization ratio measurements of mineral, sea-salt, and ammonium sulfate particles simulated in a laboratory chamber. Appl Opt 49:4441. https://doi.org/10.1364/AO.49.004441

Schnaiter M, Büttner S, Möhler O, Skrotzki J, Vragel M, Wagner R (2012) Influence of particle size and shape on the backscattering linear depolarisation ratio of small ice crystals-cloud chamber measurements in the context of contrail and cirrus microphysics. Atmos Chem Phys 12:10465–10484. https://doi.org/10.5194/acp-12-10465-2012

Seinfeld JH, Pandis SN (2006) Atmospheric chemistry and physics: from air pollution to climate change, 2nd edn. J. Wiley, Hoboken, N.J

Shakya KM, Peltier RE (2015) Non-sulfate sulfur in fine aerosols across the United States: insight for organosulfate prevalence. Atmos Environ 100:159–166. https://doi.org/10.1016/j.atmosenv.2014.10.058

Shakya KM, Peltier RE (2013) Investigating missing sources of sulfur at fairbanks. Alaska Environ Sci Technol 47:9332–9338. https://doi.org/10.1021/es402020b

Stier P, Seinfeld JH, Kinne S, Boucher O (2007) Aerosol absorption and radiative forcing. Atmos Chem Phys 25

Studinski RC, Vitkin IA (2000) Methodology for examining polarized light interactions with tissues and tissuelike media in the exact backscattering direction. J Biomed Opt 5:330–337. https://doi.org/10.1117/1.430004

Surratt JD, Gómez-González Y, Chan AWH, Vermeylen R, Shahgholi M, Kleindienst TE, Edney EO, Offenberg JH, Lewandowski M, Jaoui M, Maenhaut W, Claeys M, Flagan RC, Seinfeld JH (2008) Organosulfate formation in biogenic secondary organic aerosol. J Phys Chem A 112:8345–8378. https://doi.org/10.1021/jp802310p

Tesche M, Ansmann A, Müller D, Althausen D, Engelmann R, Freudenthaler V, Groß S (2009) Vertically resolved separation of dust and smoke over Cape Verde using multiwavelength Raman and polarization lidars during Saharan Mineral Dust Experiment 2008. J Geophys Res 114. https://doi.org/10.1029/2009JD011862

Tesche M, Kolgotin A, Haarig M, Burton SP, Ferrare RA, Hostetler CA, Mueller D (2019) 3+2 + X: what is the most useful depolarization input for retrieving microphysical properties of non-spherical particles from lidar measurements using the spheroid model of Dubovik et al. (2006)

Tolocka MP, Turpin B (2012) Contribution of organosulfur compounds to organic aerosol mass. Environ Sci Technol 46:7978–7983. https://doi.org/10.1021/es300651v

van de Hulst HC (1957) Light scattering by small particles. Courier Corporation

Veselovskii I, Goloub P, Podvin T, Bovchaliuk V, Derimian Y, Augustin P, Fourmentin M, Tanre D, Korenskiy M, Whiteman DN, Diallo A, Ndiaye T, Kolgotin A, Dubovik O (2016) Retrieval of optical and physical properties of African dust from multiwavelength Raman lidar measurements during the SHADOW campaign in Senegal. Atmos Chem Phys 16:7013–7028. https://doi.org/10.5194/acp-16-7013-2016

Videen G, Muinonen K (2015) Light-scattering evolution from particles to regolith. J Quant Spectrosc Radiat Transf 150:87–94. https://doi.org/10.1016/j.jqsrt.2014.05.019

Videen G, Zubko E, Arnold JA, MacCall B, Weinberger AJ, Shkuratov Y, Muñoz O (2018) On the interpolation of light-scattering responses from irregularly shaped particles. J Quant Spectrosc Radiat Transf 211:123–128. https://doi.org/10.1016/j.jqsrt.2018.03.009

Vitkin IA, Studinski RCN (2001) Polarization preservation in diffusive scattering from in vivo turbid biological media: effects of tissue optical absorption in the exact backscattering direction. Opt Commun 190:37–43

Volten H, Muñoz O, Rol E, de Haan JF, Vassen W, Hovenier JW, Muinonen K, Nousiainen T (2001) Scattering matrices of mineral aerosol particles at 441.6 nm and 632.8 nm. J Geophys Res 106:17375. https://doi.org/10.1029/2001JD900068

Wang X, Lai J, Li Z (2012) Polarization studies for backscattering of RBC suspensions based on Mueller matrix decomposition. Opt Express 20:20771

Wiersma DS, Bartolini P, Lagendijk A, Righini R (1997) Localization of light in a disordered medium. Nature 390:671–673. https://doi.org/10.1038/37757

Winker DM, Pelon JR, McCormick MP (2003) The CALIPSO mission: spaceborne lidar for observation of aerosols and clouds. In: Singh UN, Itabe T, Liu Z (eds) Presented at the Third international asia-pacific environmental remote sensing remote sensing of the atmosphere, ocean, environment, and space, Hangzhou, China, p. 1. https://doi.org/10.1117/12.466539

Zhang Y, Chen Y, Lambe AT, Olson NE, Lei Z, Craig RL, Zhang Z, Gold A, Onasch TB, Jayne JT, Worsnop DR, Gaston CJ, Thornton JA, Vizuete W, Ault AP, Surratt JD (2018) Effect of the Aerosol-Phase State on secondary organic aerosol formation from the reactive uptake of isoprene-derived epoxydiols (IEPOX). Environ Sci Technol Lett 5:167–174. https://doi.org/10.1021/acs.estlett.8b00044

Zong R, Weng F, Bi L, Lin X, Rao C, Li W (2021) Impact of hematite on dust absorption at wavelengths ranging from 0.2 to 1.0 μm: an evaluation of literature data using the T-matrix method. Opt Express 29:17405–17427. https://doi.org/10.1364/OE.427611

Zubko E, Muinonen K, Muñoz O, Nousiainen T, Shkuratov Y, Sun W, Videen G (2013) Light scattering by feldspar particles: comparison of model agglomerate debris particles with laboratory samples. J Quant Spectrosc Radiat Transf 131:175–187. https://doi.org/10.1016/j.jqsrt.2013.01.017

Zubko E, Muinonen K, Shkuratov Y, Videen G, Nousiainen T (2007) Scattering of light by roughened Gaussian random particles. J Quant Spectrosc Radiat Transf 106:604–615. https://doi.org/10.1016/j.jqsrt.2007.01.050